Elsevier Editorial System(tm) for Chemical Geology
Manuscript Draft

Manuscript Number: CHEMGE6928R1

Title: Quantifying chemical weathering intensity and trace element release from two contrasting basalt profiles, Deccan Traps, India

Article Type: Research Article

Keywords: Deccan Traps, weathering index, mafic index of alteration, index of lateritisation, Sm/Nd, europium anomaly, dust

Corresponding Author: Mr. Michael Gordon Babechuk,

Corresponding Author's Institution: Trinity College Dublin

First Author: Michael Gordon Babechuk

Order of Authors: Michael Gordon Babechuk; Mike Widdowson; Balz S Kamber

Abstract: Weathering profiles developed on basalt substrate contain information relevant to climate, atmospheric composition and evolution, nutrient release into the hydrosphere, and understanding Martian regolith. In this study, the chemical compositions of two profiles developed on Deccan Trap basalt are examined. One is sub-Recent and has only progressed to a moderate degree of alteration (Chhindwara profile), whereas the other is ancient (Paleocene) and the degree of alteration is extreme (Bidar laterite). In an attempt to better quantify the chemical changes during incipient to intermediate weathering of mafic substrates, we propose a new index: the mafic index of alteration (MIA). Similar to the chemical index of alteration (CIA), the MIA quantifies the net loss of the mobile major elements (Ca, Mg, Na, K ± Fe) relative to the immobile major elements (Al ± Fe). The redox-dependent weathering behaviour of Fe is factored into two separate arrangements of the MIA that apply to oxidative [MIA(O)] or reduced [MIA(R)] weathering. The MIA can be visualised in a variety of ternary diagrams in the Al-Fe-Mg-Ca-Na-K system. To chemically quantify the stages of advanced to extreme weathering, at which the MIA and CIA are ineffective, the SiO_2 to (Al_2O_3+Fe_2O_3) mass ratio, based on the established Si-Al-Fe (SAF) 'laterite' ternary diagram, is used; we propose that this ratio be referred to as the 'index of lateritisation' (IOL).

Major element chemical variations, as expressed by weathering indices, were used to relate the extent of weathering with the behavior of trace elements (alkali, alkaline earth, rare earth, and Nb) in the profiles. During the early stages of basalt weathering, the mobile trace elements (Sr, Be, Li) are anti-correlated with the chemical weathering indices and thus released during these stages. By contrast, the monovalent elements (K, Rb, Cs, Tl), excluding Na and Li, appear to be associated with the pedogenetic clay minerals. Of these elements, those with the closest ionic radii are most closely related. Fractionation of the REE (Sm/Nd, Eu/Eu*, Ce/Ce*) is evident during weathering of the basalt. The loss of Eu is linked with Sr, Ca, and Na and thus plagioclase dissolution during the stages of incipient to intermediate weathering. The fractionation of Sm/Nd suggests that basaltic weathering products may not always preserve their parent rock ratio and, consequently, their Nd isotope composition over time.

Finally, weathering in the sub-Recent profile is shown to have progressed across two lava flows, whose morphology initially controlled the extent of weathering. Certain compositional variations in the

original flows (e.g., immobile element ratios) are preserved through the effects of chemical weathering and have the potential to influence mass balance calculations across the entire profile.

CHEMGE6928 highlights

- New chemical weathering index is introduced: the mafic index of alteration (MIA)
- Si:(Si+Fe+Al) ratio to quantify advanced weathering (the index of lateritisation)
- Separate lava flows in a weathering profile influence mass balance calculations
- REE fractionation during basalt weathering: LREE/HREE, Sm/Nd, Ce/Ce*, Eu/Eu*

Quantifying chemical weathering intensity and trace element release from two contrasting basalt profiles, Deccan Traps, India

Babechuk, M.G.*[a,b], Widdowson, M.[c], Kamber, B.S.[b]

a. Department of Earth Sciences, Laurentian University, Sudbury, P3E 2C6, Canada

b. Department of Geology, Trinity College Dublin, Dublin 2, Ireland

c. Department of Environment, Earth and Ecosystems, The Open University, Milton Keynes, MK7 6AA, UK

*Corresponding author contact information:

Phone: +353 (0)1 896 2675

Fax: +353 (0)1 6711199

Email: babechmg@tcd.ie

ABSTRACT

Weathering profiles developed on basalt substrate contain information relevant to climate, atmospheric composition and evolution, nutrient release into the hydrosphere, and understanding Martian regolith. In this study, the chemical compositions of two profiles developed on Deccan Trap basalt are examined. One is sub-Recent and has only progressed to a moderate degree of alteration (Chhindwara profile), whereas the other is ancient (Paleocene) and the degree of alteration is extreme (Bidar laterite). In an attempt to better quantify the chemical changes during incipient to intermediate weathering of mafic substrates, we propose a new index: the mafic index of alteration (MIA). Similar to the chemical index of alteration (CIA), the MIA quantifies the net loss of the mobile major elements (Ca, Mg, Na, K ± Fe) relative to the immobile major elements (Al ± Fe). The redox-dependent weathering behaviour of Fe is factored into two separate arrangements of the MIA that apply to oxidative [$MIA_{(O)}$] or reduced [$MIA_{(R)}$] weathering. The MIA can be visualised in a variety of ternary diagrams in the Al–Fe–Mg–Ca–Na–K system. To chemically quantify the stages of advanced to extreme weathering, at which the MIA and CIA are ineffective, the SiO_2 to (Al_2O_3+Fe_2O_3) mass ratio, based on the established Si–Al–Fe (SAF) 'laterite' ternary diagram, is used; we propose that this ratio be referred to as the 'index of lateritisation' (IOL).

Major element chemical variations, as expressed by weathering indices, were used to relate the extent of weathering with the behavior of trace elements (alkali, alkaline earth, rare earth, and Nb) in the profiles. During the early stages of basalt weathering, the mobile trace elements (Sr, Be, Li) are anti-correlated with the chemical weathering indices and thus released during these stages. By contrast, the monovalent elements (K, Rb, Cs, Tl), excluding Na and Li, appear to be associated with the pedogenetic clay minerals. Of these elements, those with the closest ionic

radii are most closely related. Fractionation of the REE (Sm/Nd, Eu/Eu*, Ce/Ce*) is evident during weathering of the basalt. The loss of Eu is linked with Sr, Ca, and Na and thus plagioclase dissolution during the stages of incipient to intermediate weathering. The fractionation of Sm/Nd suggests that basaltic weathering products may not always preserve their parent rock ratio and, consequently, their Nd isotope composition over time.

Finally, weathering in the sub-Recent profile is shown to have progressed across two lava flows, whose morphology initially controlled the extent of weathering. Certain compositional variations in the original flows (e.g., immobile element ratios) are preserved through the effects of chemical weathering and have the potential to influence mass balance calculations across the entire profile.

Keywords: Deccan Traps, weathering index, mafic index of alteration, index of lateritisation, Sm/Nd, europium anomaly

HIGHLIGHTS

- New chemical weathering index is introduced: the mafic index of alteration (MIA)
- Si:(Si+Fe+Al) ratio to quantify advanced weathering (the index of lateritisation)
- Separate lava flows in a weathering profile influence mass balance calculations
- REE fractionation during basalt weathering: LREE/HREE, Sm/Nd, Ce/Ce*, Eu/Eu*

1. INTRODUCTION

Chemical breakdown of thermodynamically unstable minerals at the Earth's surface by weathering agents is a fundamental part of global elemental cycles. It is responsible for the long-term regulation of global atmospheric CO_2 concentrations and for generating clastic sediment and dissolved elements for delivery to fluvial and marine reservoirs. Therefore, in view of this critical role, it is perhaps not surprising that several geochemical indices have been introduced for the purpose of understanding and quantifying the processes of weathering (e.g., Parker, 1970; Kronberg and Nesbitt, 1981; Nesbitt and Young, 1982; Harnois, 1988; Maynard, 1992; Fedo et al., 1995; Retallack, 2001 and references therein; Ohta and Arai, 2007; Sheldon and Tabor, 2009; Nordt and Driese, 2010). Such quantification of the degree of weathering in soils/paleosols or clastic sedimentary sequences has proven important from the scale of an individual weathering profile up to that of global mass balance. At the scale of an individual weathering profile, the most useful weathering indices are those with elemental components that can be determined routinely and examined graphically to provide further insight into the weathering and/or post-weathering processes. One of the most widely used examples is the chemical index of alteration (CIA: Nesbitt and Young, 1982, 1984, 1989) and the accompanying A–CN–K diagram (Nesbitt and Young, 1984; Fedo et al., 1995).

In this study, a new chemical weathering index modelled after the CIA is introduced: the mafic index of alteration (MIA). The MIA adds the elements Fe and Mg to the Al–Ca–Na–K system, allowing the mafic mineral component of rock weathering to be quantified. The MIA is most suitable for, but not restricted to, studying mafic rock weathering. The study of chemical weathering of mafic substrates, compared to felsic substrates, provides many advantages from a geological and chemical perspective: a) the parent rock is often fine-grained and typically quite

homogeneous from a chemical and mineralogical perspective; b) the substrate is quite rich in redox-sensitive elements, such as the transition metals; c) basalt or its metamorphosed/altered equivalent is ubiquitous throughout the known geological record, and e) it is of increasing importance for interpreting Martian substrate alteration. Silicate weathering is perhaps the most important removal mechanism of CO_2 from the atmosphere, with the weathering of mafic substrates often being cited as especially important in the regulation of global climatic changes (Louvat and Allègre, 1997; Schwarz, 1997; Gaillardet et al., 1999; Taylor and Lasaga, 1999; Dessert et al., 2001; Das et al., 2005; Navarre-Sitchler and Brantley, 2007).

Although the major elements closely reflect the mineralogical transformations during weathering, the cycling of certain minor and trace elements has potential to provide further insight into pedogenetic processes, such as biological activity or the oxidation state of a profile. Linking the release or retention of these elements to specific stages of chemical weathering can be accomplished through the combined use of major element weathering indices and trace element mass balance. In this study, this is demonstrated for the alkali, alkaline earth, and rare earth elements during different stages of alteration of the Deccan Traps basalt.

2. BASALT CHEMICAL WEATHERING AND LATERITISATION

2.1. Incipient to intermediate weathering

For typical basaltic rocks, the susceptibility of minerals to chemical weathering follows the order of glass ≈ olivine > plagioclase ≈ pyroxene > Fe-Ti oxide (e.g., Eggleton et al., 1987; Nesbitt and Wilson, 1992), although some exceptions related to particular textural characteristics or the weathering environment have been reported (e.g., Craig and Loughnan, 1964). Ultimately,

pedogenetic phyllosilicates (e.g., kaolinite and the smectite group minerals) and Fe and Mn oxides or oxyhydroxides form from the primary basaltic constituents during weathering. The exact pedogenetic mineralogy and order of mineral formation depend on the parent rock composition, climate, biology, redox state, and drainage of the profile (e.g., Prudêncio et al., 2002; Rasmussen et al., 2010). During the incipient to early stages of basalt weathering, 2:1 layer phyllosilicates typically form and significant hydration occurs. As weathering progresses from to intermediate and advanced stages, 1:1 layer clays such as kaolinite or halloysite are typical stable end-products. Therefore, this realm of chemical weathering is sometimes referred to as 'kaolinitisation'.

During the early stages of basalt weathering, a general net loss of the mobile elements (Mg, Ca, Na, ± K) accompanies the mineralogical transformations (e.g., Nesbitt et al., 1980; Chesworth et al., 1981; Kronberg and Nesbitt, 1981). By contrast, Al, Fe, and Si are predominantly retained. Therefore, quantification of weathering intensity during these stages typically assumes conservation of Al and measures the loss of the mobile elements (Ca, Na, K, Mg). The weathering behaviour of Fe, however, may be more complicated and dependent on the redox and drainage conditions of the profile (e.g, Driese, 2004).

2.2. Advanced to extreme weathering and lateritisation

The term 'laterite' comes with a history of debate and disagreement related to the origin of duricrusts (for recent discussion see Ollier and Galloway, 1990; Bourman, 1993; Bourman and Ollier 2002, 2003; Schellmann, 2003). We prefer to adopt the genetic distinction between ferricrete and laterite (e.g., Aleva, 1994; Widdowson, 2007); in this study, 'lateritisation' will refer to the progressive, *in situ* alteration of rock. By contrast, ferricretes are alteration profiles

that are largely generated by the allochthonous input and accumulation of ferruginous cement within existing subaerial substrates. In practice, the distinction between laterite and ferricrete cannot always be readily made in the field, and may require very detailed characterisation of duricrusts (e.g., Beauvais, 1999). Genetic distinctions are further complicated on a smaller scale since even *in situ* weathering profiles are subject to some lateral element transfer and the incorporation of aeolian sediment (Figure 1).

Lateritisation is generally associated with intense and prolonged leaching conditions in sufficiently hot and humid climates. During advanced to extreme weathering that is associated with lateritisation, the stage of pedogenetic phyllosilicate accumulation is exceeded and Fe- and Al-oxyhydroxides and sesquioxides (e.g., gibbsite, goethite, hematite) begin to dominate the weathering profile mineralogy. The Si largely retained in the phyllosilicates during earlier stages of weathering is lost (e.g., Widdowson and Gunnell, 1999; Hill et al., 2000) and desilication becomes the dominant process modifying the chemistry of the weathering profile. In this respect, the classic chemical definition of 'laterite' by Schellmann (1981, 1982, 1986) based on the SiO_2 to (Fe_2O_3 + Al_2O_3) ratio becomes useful in accompanying field observations of lateritic profiles. This ratio and the accompanying SiO_2–Al_2O_3–Fe_2O_3 (SAF) ternary plot provide a quantifiable chemical criterion to examine highly altered substrates, although they are not applicable to allochthonous duricrusts (i.e., ferricretes). The full progression of chemical weathering must be recorded within a single 'laterite profile' that is characterised by a gradual alteration of parent rock to saprolite near the base and grading into a pallid zone, followed by a mottled zone, and finally an indurated, Fe-rich duricrust at the top (i.e., the 'textbook' laterite profile). Caution should be exercised where an *in situ* progressive weathering profile cannot be unequivocally identified or where the parent rock is unavailable or unknown.

3. GEOLOGY

3.1 Geological and geochemical context of the Deccan Volcanic Province

The Deccan Volcanic Province (DVP), located in western peninsular India, is the remnant of an extensive, continental flood basalt emplaced during a tholeiitic eruptive acme between ca. 67-65 Ma (e.g., Duncan and Pyle, 1988; Gallet et al., 1989; Widdowson et al., 2000; Hofmann et al., 2000; Chenet et al., 2007; Hooper et al., 2010) at the Cretaceous-Paleogene Boundary (KPgB). Immediately following the eruption of the Deccan Traps flood basalt, the neo-formed lava fields were exposed to intense tropical weathering due to the equatorial location of the DVP around the KPgB. Accordingly, deep (lateritised) weathering profiles developed uninterrupted throughout the Paleocene. The weathering intensity is likely to have waned in the Eocene following continental uplift resulting from the collision of the Indian and Asian plates and/or denudational uplift of the rifted margin of Western India (65-50 Ma; Beck et al., 1995; Widdowson, 1997); this, together with climate changes resulting from the closure of the Tethyan seaway and later uplift of the Himalayas, and associated profound alteration of Indian continental drainage patters, are likely to have resulted in changes in Indian weathering regimes (e.g., Kerrick and Caldeira, 1993).

Remnants of Paleocene and Miocene duricrusts are found located at topographical highs in the Western Ghats and across the low-lying Konkan coastal plain, respectively (Widdowson and Cox, 1996; Widdowson, 1997). The high-level duricrusts are interpreted as remnants of the once extensive weathering residuum that had developed on the top of the DVP lava flow package after eruptions had ceased (ca. 60 Ma), whilst the low-lying examples of the Konkan plain represent

alteration of a piedmont-like paleosurface developed at the foot of the Western Ghats escarpment in the upper Tertiary (e.g., Widdowson and Gunnell, 1990; Widdowson, 2007).

Differential weathering and erosion of the flat-lying basaltic flows (c. 4-10 m thick) has produced spurs, ridges and mesas that are separated by flat-floored valleys often containing meandering rivers. East of the Ghats escarpment these rivers drain eastward and southward eventually discharging into the Bay of Bengal, while those that drain the escarpment and Konkan plain flow westward into the Arabian Sea. Increased aridity during the LGM resulted in reduced stream flow magnitudes in the rivers of south and SE Asia, whilst the glacially-induced eustatic low extended river courses across exposed coastal plains. As wetter (monsoon) conditions returned in the early Holocene, the rivers in peninsular India responded by deepening and enlarging their channels to accommodate increased discharge leading to widespread erosion and development of river terraces (e.g., Clift et al., 2002, Kale, 2002; Figure 2). In most areas, these fluvial processes stripped the deeply lateritised Paleocene duricrust and exposed fresh basalt in topographical lows to Holocene weathering. Therefore, most of the current outcrop of the DVP (> 90%) consists of basalt variably weathered to 1 to 10 m in a stepped mesa-like topography that is largely the result of Quaternary (Pleistocene-Holocene) fluvial processes of valley incision and widening in the wake of the last glacial maximum (LGM).

The DVP provides an ideal natural laboratory to study the various stages of chemical weathering of compositionally similar tholeiitic basalt. The thick, near horizontal geometry of the DVP flows and the mesa topography of the area has ensured that the current chemical state of the weathering profiles has been isolated from interaction with ground or surface waters. Further, given the massive areal extent of the DVP flows, the study sites are remote from other basement lithology and only minor aeolian input could possibly interfere with the DVP's excellent

potential for investigating basaltic chemical weathering (Kisakürek et al., 2004; Wimpenny et al., 2007).

In the present study, two weathering profiles from the eastern DVP, representing very different stages of basalt alteration, are examined. The first is an ancient (Paleocene), highly advanced (lateritic) weathering profile developed in the Bidar area (BB sample series). The second is a post-Pleistocene (sub-Recent) weathering profile located in a roadside quarry near Chhindwara (ChQ sample series) in the Madhya Pradesh district. This profile is substantially less advanced in its degree of alteration, lacking any duricrust development. The geology and sampling strategies of these two chemically different weathering profiles are summarised next and illustrated in Figure 3.

3.2. Bidar profile

The Bidar laterite profile is well exposed at a hillside edge of a mesa near Bidar, Madhya Pradesh, India (17°54.87' N, 77°32.39' E; Figure 2). This site is where Newbold (1844, 1846) first suggested laterite to be the consequence of *in situ* rock weathering. The Bidar laterite, sampled in 1998, is interpreted as a deep (~50 m) weathering profile with upwardly increasing alteration and concomitant Fe-enrichment (Borger and Widdowson, 2001; Kisakürek et al., 2004). Between the top and bottom of the profile there is a typical lateritic weathering progression, including a mottled zone, and an indurated duricrust cap (Figure 3a). The unweathered basalt (at a profile depth of > 40 m) gradationally gives way to a corestone-rich horizon and saprolite matrix between a depth of 35-30 m. This depth range is characterised by the typical depletion of mobile alkaline and alkaline earth elements that is associated with incipient weathering. Between 30-25 m, saprolite with Fe-rich mottles and segregations becomes

dominant. Above this point, primary silicates have been completely removed from the profile and Si and Al concentrations decrease relative to Fe. This is associated with an increase in the abundance of irregular Fe-rich agglomerations and a reddening of the saprolite colour upward between ~25-15 m. An unexpected return to bluish-grey saprolite between ~15-10 m marks the only apparent discontinuity in the upward weathering progression. Based on higher than expected Fe concentrations and trace metal accumulation, Kisakürek et al. (2004) argued that this horizon represents the position of a stable paleo-water table. At the highest, and most advanced part of the weathering profile, tabular, semi-indurated laterite at ~10-4 m grades into an indurated laterite cap (4 m and up). Further details of the profile geology are described in Borger and Widdowson (2001) and Widdowson (2007).

Nine samples (BB1-BB9) were collected from the Bidar laterite for previous studies (Mason et al., 2000; Kisakürek et al., 2004; Wimpenny et al., 2007), each representative of zones of key textural change. The focus during the sampling was on the uppermost transition from saprolite to laterite and on representing the various mineralogical and textural changes in the upper, most highly weathered part of the profile. Approximately 1-3 kg of material was taken for each sample to minimise the vertical and horizontal heterogeneity that is common in deeply weathered laterite profiles. The same samples were used for the present study (Figure 3a).

3.3. Chhindwara profile

The Chhindwara District is situated on a 600-750 m elevation basaltic plateau that extends approximately 200 km NE from the Seoni-Chhindwara area toward Jabalpur (Figure 2). Throughout the area, terraced hillsides or low mesas of 50-100 m elevation are separated by flat-floored valleys containing ephemeral rivers draining eastward and southward. The higher

247 elevation duricrust cap common to the Bidar area is absent. A transect through the Quaternary
248 weathering front, located in a recently abandoned road stone quarry, 7 km east of Chhindwara
249 (22° 04.213' N; 79° 01.393' E; Figure 2) was sampled in 2009; see field photographs (Figure 4).

250 Located at 741 m elevation, the weathering profile extends to a total exposed depth of >6 m
251 across two clearly identifiable massive lava flows exposed in the face of the quarry (Figure 4a).
252 Stratigraphically and geochemically, the two flows appear to belong to the Poladpur-Ambenali
253 formation transition zone (Mitchell and Widdowson, 1991). In general, the flow-banded and
254 higher vesicularity areas of both flows are more altered than the thicker, massive regions. This
255 implies that the primary flow morphology has had a strong control on fluid penetration, chemical
256 attack, and, consequently, chemical weathering intensity.

257 The fully exposed (~4 m) upper flow (ChQB) has weathered to a rust red colour with spheroidal
258 weathering features present throughout and is capped by a thin (~20 cm) soil horizon at the
259 present day surface (Figure 4). The more massive, homogeneous basalt that constitutes most of
260 the flow grades into a zone of weak 'banding' at the base (lower 80 cm), which may relate to
261 rheological effects during emplacement and/or minor mineralogical variation. The weathering
262 intensity in the flow, as indicated by the clay content, follows the aforementioned morphology
263 transition, with a sharp increase in phyllosilicates near the base that is coincident with the
264 appearance of the banded texture.

265 The transition from the upper to lower flow unit is clearly identifiable by the grayish colour of
266 the latter. The colour is presumably a result of the higher abundance of pedogenetic clays and
267 zeolite minerals. In this flow, vesicularity, made evident from zeolite-infilled amygdules,
268 increases towards the flow top and terminates with a brecciated and highly vesicular flow top (~

20 cm). The base of the lower flow is not exposed beyond the quarry floor. The colour and clay mineralogy are relatively consistent throughout the exposed portion (215 cm) of the lower flow, and suggests a higher (relative to the upper flow) but relatively consistent intensity of weathering. The difference in colour (from the rust red to brown to the greenish-gray) between the upper and lower flows could also indicate that the latter records an earlier weathering history. That is, it may represent a bole bed that formed during a period of volcanic quiescence in the DVP emplacement history (Ghosh et al., 2006; Sayyed and Hundekari, 2006) prior to the eruption of the upper flow. In addition, the presence of zeolite minerals in Deccan basalt is thought to have some control on the chemical weathering progression by retaining elements and inhibiting complete kaolinitisation (Bhattacharyya et al., 1999).

From the Chhindwara profile, a total of 27 samples were collected. The upper flow (ChQB1-B12) and lower flow (ChQA1-A12) are represented by 12 samples each and the remaining samples are from a horizontal profile through a corestone at a depth of 90 cm from the upper flow surface (ChQB9a,b,c,d; Figure 4b). The least-weathered samples of the profile, ChQB12 and ChQB9d, are located in the upper flow at a depth of 140 cm and within the corestone centre, respectively. The sample locations are indicated on a schematic log (Figure 3).

4. METHODOLOGY AND ANALYSIS

4.1. Analytical details

Samples for the Chhindwara profile were pulverised in an agate mill to minimise metal contamination, whereas the powders for the Bidar profile were prepared in a tungsten carbide mill. The major element composition for both profiles was determined by X-ray fluorescence

(XRF) following loss on ignition (LOI) measurement; the Bidar XRF data were obtained at the Open University (UK) and reported previously (Kisakürek et al., 2004; Widdowson, 2007), while the Chhindwara samples were analysed at the Geoscience Laboratories (Sudbury, Ontario). Ferrous iron measurements were also obtained on Chhindwara samples at the Geoscience Laboratories via potentiometric titration with potassium permanganate.

All trace element data were obtained in the Department of Earth Sciences at Laurentian University. A 100 mg powder aliquot was digested in thoroughly cleaned 29 mL PFA screw-top beakers using a 2.5 ml HF plus 0.5 ml HNO_3 acid mixture. After a 72 h digestion period at 160ºC, samples were dried down at 110ºC to drive off SiF_4. The fluoride residue was attacked twice with 0.5 mL 6 N HCl to reduce organic components before double conversion with HNO_3. The converted residue was taken up in 10 g of 20% HNO_3 to yield a nominal 1:100 parts total dissolved solids stock solution. This was transferred to a clear polystyrene test tube and centrifuged to inspect for insoluble fluorides, which were not encountered.

For the trace element analysis, 0.2 g (i.e., 2%) of the stock solution was gravimetrically diluted to 6 g 2% HNO_3 together with a mixture of internal standards (10.6 ppb ^{6}Li, 4.4 ppb each Rh, Re and Bi and 1.5 ppb ^{235}U). A total of 46 trace elements were analysed by quadrupole ICP-MS (Thermo XSeriesII) using the methodology of Eggins et al. (1997) with some modifications (Kamber et al., 2003; Kamber, 2009). Calibration of analyses was performed using the USGS standard W-2 digested under the same conditions as the experiment unknowns using the preferred values reported previously (e.g., Babechuk et al., 2010). Long-term reproducibilities for most elements with this method are between 1-2% (e.g., Kamber, 2009; Babechuk et al., 2010; Marx and Kamber, 2010). The major element and trace element data set relevant to the present study is reported for the Bidar profile in Table 1 and the Chhindwara profile in Table 2.

5. RESULTS AND DISCUSSION – PART I

Major elements, loss on ignition, and quantification of the extent of weathering

In the following sections, the bulk major element trends of the Bidar and Chhindwara weathering profiles are interpreted using the widely recognised chemical index of alteration (Section 5.1), as well as the new mafic index of alteration and index of lateritisation (Sections 5.2 and 5.3). A useable spreadsheet that demonstrates the weathering index calculations can be found in the supplementary materials. Each weathering index is also discussed on accompanying ternary diagrams that allow for the graphical interpretation of the proportional chemical changes. Included in ternary plots for comparison is a data compilation of published sub-Recent basaltic weathering profiles and Tertiary basaltic laterite and bauxite profiles (Chesworth et al., 1981; Eggleton et al., 1987; Marsh, 1991; Price et al., 1991; Nesbitt and Wilson, 1992; Karrat et al., 1998; Rudnick et al., 2004; Retallack, 2008; Oh and Richter, 2005; Hausrath et al., 2011; Sanematsu et al., 2011; Liu et al., 2013). In Section 5.4, correlations of the weathering indices with the loss on ignition further demonstrate the mineralogical transformations that dictate the chemical weathering trends.

5.1. The chemical index of alteration (CIA)

5.1.1 Quantifying the intensity of weathering with the CIA

Most igneous rocks of varying composition will plot between a CIA value of 35 and 50, with mafic rocks occupying the lower values. Similar to other basalts, the least-weathered (parent rock) samples of both the Chhindwara and Bidar profiles yield a CIA value of ~35.

During chemical weathering, the values of weathering indices increase due to the loss of mobile elements relative to an element assumed to be immobile. The CIA predominantly tracks feldspar dissolution and the concomitant release of Ca, Na, and K relative to Al, since the latter is typically retained within pedogenetic clays. This is evident in the clear separation of the CIA values of primary minerals (e.g., plagioclase, pyroxene: 50 and under) from those of pedogenetic minerals such as smectites, illite (70-85), and kaolinite (100).

In the Chhindwara profile, the samples extend from the unweathered CIA value of 35 to a maximum of 80 in their most altered state. This indicates that the most weathered samples of the Chhindwara profile have not yet reached complete 'kaolinitisation' and still retain a detectable amount of the labile elements (Ca, Na, and minor K), possibly due to the presence of zeolite minerals (Bhattacharyya et al., 1999). By contrast, the altered samples of the Bidar laterite profile have CIA values of 90 or greater. These high CIA values indicate the near-complete removal of labile major element cations. The CIA is ineffective at quantifying or differentiating elemental changes during the advanced stages of weathering since the dominant process occurring during lateritisation is desilication and Si is not factored into the CIA.

5.1.2 The A–CN–K diagram

The greatest strength of the CIA as a chemical weathering proxy is the utility of the accompanying A–CN–K diagram, which has empirically and kinetically predictable weathering vectors for various minerals and rock types (e.g., Nesbitt and Young, 1984; Nesbitt, 1992). The overall weathering vector for feldspar destruction in various different parent rocks is parallel or sub-parallel to the A–CN axis (e.g., Figure 5a). The precise vector direction is a function of the relative proportion of plagioclase and K-feldspar, their congruent or incongruent dissolution, and

the rate of conservation of aluminous weathering products. As predicted for basalt weathering (Nesbitt and Wilson, 1992), the majority of the Chhindwara samples follow a weathering trend that is adjacent to the A–CN join (Figure 5a). Should the degree of weathering continue, the vector is predicted to continue along the A–CN join until it reaches the A apex and the Ca, Na, and K is completely removed (complete 'kaolinitisation'). Further chemical weathering trends cannot be represented in the A–CN–K plot, as demonstrated by the Bidar laterite samples, which cluster around the A apex (Figure 5a).

5.1.3. K enrichment

A further utility of the A–CN–K plot is identifying and unravelling the effects of potassium enrichment in weathering profiles, such as the conversion of smectite group minerals to illite during diagenesis (Fedo et al., 1995). Enrichment of K results in a trend away from the weathering vector towards the K apex. This is evident in three samples located near the contact of the lower flow (ChQA) in the Chhindwara profile (K concentration of 1.7-1.8 wt. %). The position of these samples deviates from the main weathering trend in the A–CN–K plot defined by the remainder of the profile (Figure 5a). The significance of these samples is discussed further in Section 6.2.3.

5.2. The mafic index of alteration (MIA)

5.2.1 Introduction to the MIA

The mafic index of alteration (MIA) is proposed here as a chemical weathering index that extends the equation of the CIA to include the mafic elements Mg and Fe. Many of the mafic minerals (pyroxene, olivine) are susceptible to chemical weathering, resulting in the loss of Mg from weathering profiles. The loss of Mg can be monitored independently using the Mg index

(MgI; Maynard, 1992). By contrast to Mg, the fate of Fe during the weathering of most mafic minerals is redox-dependent. In reducing environments, ferrous iron [Fe^{2+}] can be mobile and leached along with Mg during mafic mineral weathering. In oxidative weathering environments, however, Fe is usually retained by the formation of highly insoluble ferric iron [Fe^{3+}] oxides or oxyhydroxides (e.g., Driese, 2004) and thus enriched along with Al. Due to this dichotomous redox behaviour of Fe, an arrangement of the MIA is proposed for each of the end-member weathering environments.

When the alteration environment is oxidising and Fe is retained, total Fe is considered an immobile element along with Al (Al_2O_3) and the MIA calculation is:

Eq. 1: $MIA_{(O)} = 100 \times [(Al_2O_3 + Fe_2O_{3(T)}) / (Al_2O_3 + Fe_2O_{3(T)} + MgO + CaO^* + Na_2O + K_2O)]$

When the alteration environment is reducing and Fe is leached along with Mg, total Fe is considered a mobile element along with Mg, Ca, and K and the MIA calculation is:

Eq. 2: $MIA_{(R)} = 100 \times [Al_2O_3 / (Al_2O_3 + Fe_2O_{3(T)} + MgO + CaO^* + Na_2O + K_2O)]$

In both arrangements of the MIA [$MIA_{(O)}$ or $MIA_{(R)}$], increasing index values represent progressively more altered rock, as is the case with the CIA. A value of 100 indicates complete removal of the mobile elements. As with the CIA, the MIA uses the molar ratios of the major element oxides by converting the wt. % concentrations into moles (see Table 3). The molar CaO is corrected for the presence of carbonate and apatite as for the CIA (e.g., Fedo et al., 1995) to consider only the silicate-bound Ca (CaO*).

In addition to the index value, the proportional changes of the elements in the MIA can be studied graphically with ternary plots in the Al–Fe–Mg–Ca–Na–K system (e.g., Nesbitt and

Young, 1989; Nesbitt and Wilson, 1992) whereby both versions of the MIA are arranged into the plots in the same manner as the CIA with the A–CN–K diagram. The $MIA_{(R)}$ arranges into the Al_2O_3–($CaO^* + K_2O + Na_2O$)–($Fe_2O_{3(T)} + MgO$) (A–CNK–FM) plot (Nesbitt and Young, 1989), while the $MIA_{(O)}$ arranges into the Al_2O_3–($CaO^* + MgO + Na_2O + K_2O$)–$Fe_2O_{3(T)}$ (A–L–F) plot (Nesbitt and Wilson, 1992) as well as the newly proposed ($Al_2O_3 + Fe_2O_{3(T)}$) –($CaO^* + Na_2O + K_2O$)–MgO (AF–CNK–M) plot. The details of these plots are presented in Sections 5.2.3-5.2.5.

It needs to be cautioned that the MIA calculation values and the trends in ternary plots will vary slightly depending on the use of FeO or Fe_2O_3 for total Fe due to the cation mole difference. The factor for converting between FeO wt. % and Fe_2O_3 wt. % is shown in Table 3. Either oxide can be applied in the MIA, but consistency should be used between the weathering index calculations and the ternary plots and when comparing separate data sets. In this study, the moles of Fe are calculated using the total Fe as Fe_2O_3. All literature values used were recast to total Fe expressed as Fe_2O_3 and all of the major element oxides subsequently normalised to 100% on an anhydrous basis to allow for accurate comparison.

The application of the MIA and associated ternary plots to studying weathering profiles is best accompanied with independent knowledge of the redox-related behaviour of Fe. This can be accomplished with independent tests of iron immobility or the determination of the Fe^{2+} content. For example, a ternary plot of Al_2O_3–MgO–$Fe_2O_{3(T)}$ (A–M–F) or a cross-plot of the CIA vs. $Fe_2O_{3(T)}$ can be used to examine the net behaviour of iron (i.e., retention or loss) in a weathering profile relative to Al, as demonstrated by Young (2013). Plots of total Fe vs. Ti or Al have also been used to test for iron mobility (e.g., Rye and Holland, 1998).

5.2.2 Comparison of the MIA and CIA

There is an inherent range in MIA and CIA values for unweathered igneous protoliths reflecting bulk composition (see supplementary information). For the purpose of this study, discussion is limited to mafic compositions and their weathered products. The weathering index values of several mafic USGS standards and parent rock samples from the Bidar and Chhindwara profiles are summarised in Table 4. In all cases, the $MIA_{(O)}$ values are low (less than 45) and close to the calculated CIA values. The CIA vs. $MIA_{(O)}$ values from the Bidar and Chhindwara profiles are plotted in Figure 6a along with the compilation of sub-Recent mafic and Tertiary laterite/bauxite profiles. Overall, the $MIA_{(O)}$ is only slightly lower than the CIA for the majority of samples and the data are very well correlated (r^2=0.900), confirming the similar bulk weathering behaviour of Mg, Ca, and Na. The overall correlation between the two indices is poorest between a CIA value of 60 and 85, which could indicate a slightly different behaviour of Mg from Ca and Na during pedogenetic clay formation in the intermediate weathering stages.

When examined in greater detail, it is evident that the $MIA_{(O)}$ and CIA are nearly linearly correlated in the upper flow of the Chhindwara profile (r^2=0.978; up to a CIA and MIA value of approximately 70), but decoupled in the lower flow. In the latter, the CIA continues to increase to a value of 80 while the $MIA_{(O)}$ remains relatively static between 68 and 70, suggesting a divergence in the behaviour of Mg and/or Fe from Ca and Na. The concentrations of Fe and Ti are correlated and the Fe^{2+}/Fe^{3+} ratio decreases from 2.56 to 0.03 with increasing CIA values (Figure 6b) in the entire profile, suggesting complete Fe retention via oxidative weathering. Therefore, it appears that the CIA-$MIA_{(O)}$ decoupling is most likely related to minor Mg retention in the samples from which Ca and Na are more heavily depleted, perhaps in a smectite group mineral or zeolite. Consequently, the MIA is less sensitive to the chemical changes that occur in the lower flow of the profile.

445 In the Bidar profile, the $MIA_{(O)}$ values are high and relatively invariable (from 91 to 99), similar
446 to the CIA, showing that the MIA suffers from the same inability to quantify the advanced to
447 extreme stages of weathering.

448 *5.2.3 The A–CNK–FM diagram*

449 The A–CNK–FM ternary diagram was proposed by Nesbitt and Young (1989) in order to
450 consider the mafic mineral component in rock weathering. In this plot (Figure 7a), the feldspar
451 (felsic) weathering vector should follow a direction approximately away from the CNK apex
452 through the position of the unweathered sample. The exact magnitude and direction is largely
453 influenced by the rate of feldspar weathering and the type of secondary weathering product. The
454 loss of Fe and Mg from the mafic minerals should result in a weathering vector that emanates
455 away from the FM apex through the unweathered sample. During oxidative weathering,
456 however, Fe is not typically lost from the system. This complicates the mafic weathering trends
457 and contributes to the difficulty in predicting the overall rock weathering vectors (Nesbitt and
458 Young, 1989; Nesbitt, 1992). Regardless, empirical data for Phanerozoic basalt weathering (e.g.,
459 Nesbitt and Wilson, 1992) show that progressive alteration of basalt results in a trend away from
460 the CNK apex. Such a trend is evident in the Chhindwara weathering profile (Figure 7a). Taken
461 alone, a net weathering vector emanating away from the CNK apex suggests a greater relative
462 mobility and more extensive leaching of Ca, Na, and K compared to Mg. This may be
463 misleading, however, since Mg is known to exhibits a similar bulk weathering behaviour to Ca
464 and Na (Nesbitt and Wilson, 1992). Therefore, it appears that the behaviour of Fe and Mg are not
465 accurately represented in the plot due to their contrasting behaviour in most (oxidative)
466 weathering environments. It is not until Ca, Na, and K are depleted and the stages of advanced
467 weathering are reached that change in the relative proportion of Mg, Fe and Al are recorded on

468 the A–CNK–FM plot (Nesbitt and Young, 1989). This is demonstrated by the lateritised Bidar
469 samples in Figure 7a, which fall on the A-FM axis and are a function of the relative proportion of
470 aluminous (e.g., gibbsite, kaolinite) and ferruginous (e.g., hematite, goethite) pedogenetic
471 products.

472 Our analyses suggest that the A–CNK–FM diagram is most applicable to weathering
473 environments in which Fe^{2+} is mobile and behaves like Mg during chemical weathering (i.e., in
474 reduced geochemical environments, such as recorded in Archaean and early Proterozoic
475 weathering profiles). In these environments, loss of Mg and Fe is summative and results in a
476 mafic mineral weathering vector away from FM apex. Ultimately, this would result in a net
477 weathering vector that is directed away from the CNK–FM axis towards the A apex. In this
478 scenario, the $MIA_{(R)}$ can be projected into the diagram and is equivalent to the tie-line between
479 the A–CNK and A–FM axes, as shown in Figure 7a. In oxidative weathering environments, one
480 of the two following ternary re-arrangements is more useful.

481 *5.2.4 The A–L–F diagram*

482 One solution to the competing Fe and Mg vectors of the A–CNK–FM diagram, is the A–L–F
483 diagram of Nesbitt and Wilson (1992), where Mg is moved to the same apex as Ca, Na, and K
484 (Figure 7b). These four elements comprise the total labile (L) cation content. The upper apex is
485 Al and the remaining axis becomes total Fe. In this plot, the net rock weathering vector is
486 predicted to emanate away from the L apex through the position of the unweathered sample as
487 Ca, Na, K, and Mg are lost. The magnitude of this vector represents the degree of element loss
488 during weathering. This trend is demonstrated with the Chhindwara profile and the literature
489 compilation in Figure 7b. Minor differences in the starting modal mineralogy and the exact

490 pedogenetic weathering products, however, appears to result in slightly different slopes in the
491 empirical weathering vectors. Complete loss of these elements would result in the trend reaching
492 the A–F axis. Accordingly, the $MIA_{(O)}$ value in the A-L-F plot is equivalent to the tie line joining
493 the L–A and L–F axes, with values increasing towards the A–F tie axis (MIA value of 100).

494 Although $MIA_{(O)}$ values reach a maximum at the A-F axis, one advantage of the A–L–F plot is
495 that advanced weathering trends can be graphically visualised by trends moving towards the Fe
496 apex (lateritisation) or the Al apex (bauxitisation). The proportion of the aluminous and
497 ferruginous minerals in the advanced weathering residue can be extracted from the plot based on
498 the sample position trend along the A-F axis (Nesbitt and Wilson, 1992). For example, the Bidar
499 samples plot along the A-F axis moving towards the F apex, demonstrating the Fe enrichment
500 in the profile (Figure 7b). Therefore, the plot is also useful for assessing the net behaviour of Fe
501 (i.e., enrichment or loss) during weathering in modern and ancient weathering profiles, similar to
502 the A-M-F plot (Young, 2013).

503 *5.2.5 The AF–CNK–M diagram*

504 For further assessing (oxidative) mafic weathering trends, another complementary ternary plot is
505 proposed: the AF–CNK–M ternary plot (Figure 7c). This ternary diagram is generated by a
506 simple rearrangement of Fe to the upper apex along with Al, leaving Mg to its own apex. As
507 such, the plot allows the immobile behaviour of Fe in oxidised weathering environments to be
508 separated from the typically mobile behaviour of Mg. The main advantage of this arrangement of
509 the apices is that the relative contribution of CNK (feldspar) dissolution to the overall weathering
510 vector can be compared to that of Mg loss. The net weathering vector is the summation of the
511 two independent vectors emanating away from the CNK and M apices towards the AF apex. This

is demonstrated with the literature compilation in the plot (Figure 7c). On the scale of an individual weathering profile, the starting position and exact vector direction is influenced by the proportion of mafic minerals to feldspar and the rate at which they weather relative to each other. In the AF–CNK–M plot, the MIA is equivalent to the tie line between the CNK and M apices, increasing upwards toward the AF apex (MIA value of 100).

The samples from the Chhindwara profile on the AF–CNK–M plot illustrate that plagioclase weathering (loss of Ca, Na) has exceeded mafic mineral weathering (loss of Mg), resulting in an empirical trend that is directed slightly towards the AF-M join. However, by comparison with the A–CNK–FM plot, the AF–CNK–M plot confirms that Mg does contribute significantly to the weathering vector, since the empirical trend is not directed purely away from the CNK apex. Furthermore, the AF–CNK–M emphasises the change in weathering behaviour of Mg in the lower flow of the Chhindwara profile compared to the upper flow (Section 5.2.2); in the lower flow samples, the loss of Mg appears to slow while minor Ca and Na loss continues as indicated by the change to a horizontal vector in the diagram (Figure 7c).

In the AF–CNK–M plot, advanced weathering trends converge towards the AF apex and the enrichment of an Al vs. Fe cannot be diagrammatically visualised as it can in the A–L–F plot. Therefore, all of the Bidar laterite profile samples plot at or near the AF apex at $MIA_{(O)}$ values greater than 90.

5.2.6 Extended application and limitations of the MIA

The focus of the present study is to highlight the applicability of the MIA to quantifying weathering intensity and associated chemical changes in mafic substrates. Apart from this application, the use of the MIA may extend to studying intermediate and felsic rock weathering,

sediments and sedimentary rocks, or different types of alteration. It needs to be strictly noted, however, that unweathered igneous rocks of different composition will have varying initial $MIA_{(O)}$ and $MIA_{(R)}$ values (Supplementary information). Therefore, a singular MIA value should not be used to infer the extent of weathering unless some knowledge of the parent rock to a weathering profile or sediment is known.

One of the unique applications of the MIA is for quantifying chemical weathering trends in the ancient paleosol record, since the $MIA_{(R)}$ can be applied to paleosols in which Fe is lost (anoxic paleosols), while the $MIA_{(O)}$ can be used for those in which Fe is retained (oxygenated paleosols). Similar to modern weathering environments, most Precambrian paleosols and clastic sedimentary rocks are significantly depleted in Ca and Mg and, thus, the MIA may be useful in the modelling of global chemical weathering fluxes in both the modern and ancient rock record (e.g., Kramers, 2002). Additionally, both versions of the MIA can be calculated without K (MIA-K), in a manner analogous to the CIA, to counter the effects of K metasomatism (e.g., Fedo et al., 1995; Maynard, 1992). Caution must be used when inferring chemical weathering intensity in rocks that have experienced post-weathering Fe and/or Mg mobility.

5.3 The index of lateritisation (IOL)

It is clear that the $MIA_{(O)}$ and CIA are incapable of adequately quantifying the stages of advanced chemical weathering. A different approach is required that is suited to the chemical changes in laterite or bauxite profiles. During lateritisation, dissolution of quartz and kaolinite (congruent or incongruent) and the enrichment of Fe oxides are the dominant processes, resulting primarily in a loss of Si relative to Al and Fe in the weathered residue (e.g., Widdowson and Gunnell, 1999; Hill et al., 2000).

Schellmann (1981, 1982, 1986) proposed a chemical classification of laterites based on the SiO_2:(Al_2O_3+Fe_2O_3) ratio and the SiO_2–Al_2O_3–$Fe_2O_{3(T)}$ (SAF) ternary plot to distinguish between kaolinitised, lateritised, and bauxitised weathering residues. First, a notional 'limit of kaolinitisation' for the early to intermediate stages of weathering can be calculated, which is associated with relatively minor Si loss. Desilication begins to dominate beyond this limit and a quantitative tripartite progression of the 'degrees' (i.e., weakly, moderately, and strongly) of lateritisation or bauxitisation can be made. This chemical classification, however, is not unanimously accepted (e.g., Bourman and Ollier, 2002; 2003) primarily because accurate representation of the alteration progression is premised upon the autochthony of a weathering profile (Figure 1) and there is a necessity to identify the protolith in order to complete the calculation. Therefore, there is potential of its inappropriate use without this type of thorough geological contextualisation. However, where applied in combination with careful geomorphological and geological interpretation, this method of chemical classification does offer significant insight into the alteration progression in a weathering profile (Schellmann, 2003; Widdowson, 2007). Accordingly, we promote use of the SiO_2:(Al_2O_3+Fe_2O_3) ratio and here suggest it should be referred to as the 'index of lateritisation' (IOL) or the 'index of bauxitisation' (IOB). To be consistent with the chemical classification of laterite and the SAF plot, we define the IOL using the *mass* (wt. %) ratio of SiO_2, $Fe_2O_{3(T)}$, and Al_2O_3, as shown in equation 4.

$$\text{Eq. 3: IOL} = 100 \times [(Al_2O_3 + Fe_2O_{3(T)}) / (SiO_2 + Al_2O_3 + Fe_2O_{3(T)})]$$

The IOL value is designed to directly accompany the SAF diagram, similar to the approach of Hill et al. (2000). Unweathered mafic rocks have IOL values that are generally less than 40, as demonstrated by the mafic USGS standards and the least-weathered samples in this study (Table

4); for instance, unweathered Deccan basalt (BB1) gives an IOL value of 35.7. In a similar fashion to the CIA and MIA, higher IOL values correspond to more intensely weathered samples; accordingly, the calculated IOL values for increasingly weathered samples progressively fall within the divisions of kaolinitisation, weak, moderate, and strong lateritisation, as determined from the composition of the protolith. The aforementioned divisions are calculated based on the amount of Si necessary to convert Al in the protolith into kaolin (see Widdowson, 2007, and the method given in the supplementary materials). The limit of kaolinitisation for the Deccan basalt, calculated from sample BB1, is 43% SiO_2 (Figure 5). In terms of the IOL, this division between kaolintisation and lateritisation occurs at an IOL value of 57; for reference, both BB3 and BB4 lie near this boundary (i.e., IOL value of 59 and 58, respectively).

In the Chhindwara profile, samples are restricted to IOL values of ~35-50, consistent with the modest loss of SiO_2 relative to Al_2O_3 and Fe_2O_3 during kaolinitisation. The Bidar laterite, however, extends across the kaolinitisation-lateritisation boundary and defines a clear trend towards the F apex with IOL values ranging from 57-94 (Figure 5b; Borger and Widdowson, 2001, Widdowson, 2007). The more extreme range in the IOL values is consistent with the upward increase in modal abundance of Fe oxides in the Bidar profile. As discussed previously, however, the samples BB5 and BB6 do not conform to the upward Fe-enrichment trend held by the remaining profile. These samples (~10-15 m depth; Figure 3), interpreted to represent a paleo-water table (e.g., Kisakürek et al., 2004; Widdowson, 2007), contain significantly higher Fe (and other metal) concentrations than would be expected at their stratigraphic position. Therefore, comparing the stratigraphy with the IOL may help to identify samples that do not meet the criteria for strict *in situ* formation.

5.4 Loss on ignition

The volatile content of a sample measured by the loss on ignition is considered proportional to the amount of hydrated minerals, in addition to carbonate, organic carbon, sulphur, less any mass gain from oxidation of elements during analysis. The LOI value of a fresh basalt is typically less than 3 wt. %. During chemical weathering, as the primary and largely anhydrous magmatic minerals are replaced by hydrated pedogenetic phyllosilicates (e.g., smectites, illite, kaolinite), the LOI is expected to increase. Previous studies have shown that the LOI can be a useful parameter for assessing the degree of weathering (e.g., Duzgoren-Aydin and Aydin, 2003), although the specific pedogenetic mineralogy ultimately controls the degree of hydration (Duzgoren-Aydin et al., 2002). Plotting the CIA, $MIA_{(O)}$, or IOL weathering indices of the Chhindwara and Bidar profiles against the LOI provides further insight into the pedogenetic mineralogical transformations (Figure 8).

A distinct positive correlation between the LOI (~1 to 18 wt. %) and the $MIA_{(O)}$ or CIA weathering indices is exhibited by the Chhindwara samples (Figure 8a). By contrast, the more intensely weathered samples of the Bidar profile are removed from the correlation and are less hydrated, with LOI values ranging from ~7 to 12 wt.%. Whereas this may seem counter-intuitive, the lateritised samples are dominated by gibbsite, goethite, and hematite (Kisakürek et al., 2004) which are less hydrous than the intermediate weathering products (kaolinite, smectites). The replacement of the hydrated phyllosilicates by sesquioxides of Fe and Al during lateritisation results in an inverse correlation with the LOI (Figure 8b). In effect, this observation provides mineralogical corroboration of the SAF plot since the change in weathering vector in Figure 5b effectively represents the notional ‘limit of kaolinitisation’ determined for the parent basalt.

6. RESULTS AND DISCUSSION – PART II

Mass gains and losses of the alkali and alkaline earth elements

The following sections discuss the geochemical behaviour of the alkaline earth (Section 6.1) and alkali elements (Section 6.2) during basalt weathering. The analysis employs a combination of mass balance values, element-element ratios, and the major element chemical weathering indices. Combining the independently calculated mass changes with the chemical weathering indices has the power of linking high-precision trace element data with specific stages of basalt alteration. The discussion will only consider the Chhindwara weathering profile since the elemental systematics of the Bidar laterite have previously been analysed (e.g., Kisakürek et al. 2004) and have been complicated by ancient paleo-water table changes and aeolian input (Mason et al., 2000; Kisakürek et al., 2004; Wimpenny et al., 2007). The K-enriched samples in the lower flow of the Chhindwara profile (Section 5.1.3) are discussed separately from the remaining samples in Section 6.2.3. The release or retention of elements in the profile is linked when possible with the Deccan Traps river water (Das et al., 2005) and sediment (Das and Krishnaswami, 2006, 2007) chemistry that is sourced from the DVP basaltic terrane.

For mass balance calculations, the tau (τ) mass transport model (Brimhall and Dietrich 1987; Anderson et al., 2002) is used. In this model, the concentrations (C) of elements (j) in the parent rock (p), relative to that of an immobile index element (i), are used as a normalisation to establish the mass changes in the progressively altered rock (w):

$$\text{Eq. 4: } \tau_{i,j} = \{[(C_{j,w}) / (C_{j,p})] / [(C_{i,w}) / (C_{i,p})]\}-1$$

The sample representing the parent rock of the Chhindwara weathering profile is ChQB12 (depth of 140 cm) based on its low degree of chemical alteration (CIA: 36, $MIA_{(O)}$: 38) and Nb is used the immobile index element (Widdowson and Cox, 1996). The $\tau_{Nb,j}$ values are plotted vs. depth in Figure 9. It should here be remembered that the Chhindwara profile is developed across two independent lava flows. Each flow can be fingerprinted chemically using immobile element ratios such as Al_2O_3/TiO_2; the upper flow has a mean ratio of 5.74 ± 0.35 whereby the lower flow is distinct with a mean ratio of 4.27 ± 0.19. Normalisation using the immobile element composition of the parent material in the upper flow results in minor mass balance offsets ($\tau_{Nb,j}$ values) for elements in the lower flow that are unrelated to pedogenesis. This does not significantly influence the interpretation of the mass balance changes, but a slight inaccuracy in the reported mass gains and losses is expected as a result.

6.1 Alkaline earth elements (+ Na)

The elements of the alkaline earth group are the most mobile during continental weathering (e.g., Nesbitt et al., 1980), being hosted in mineral phases most susceptible to chemical attack and, in general, incompatible in pedogenetic clays. In Figure 10, the $\tau_{Nb,j}$ values of the alkaline earth elements are plotted against the CIA and an anti-correlation exists for nearly all of the elements. The degree of element depletion (represented by the steepness of the slope) differs as a function of how closely related the behaviour of the element in question is to Na and Ca.

Within a ‘stratigraphic’ context, the degree of alkaline earth element (+ Na) depletion in the Chhindwara flows follows the visible extent of basalt alteration (Section 3.3); the $\tau_{Nb,j}$ values for the alkali elements change only minimally in the centre of the upper flow, but decrease near the modern soil surface and at the flow-banded area at the base (Figure 9). Within the lower flow,

668 the degree of depletion and CIA values are higher and increase from the deepest sample
669 (ChQA1) towards the flow contact (ChQA10-12) in parallel with the vesicle (amygdule)
670 abundance. The overall weathering behaviour of the alkaline earth elements (+ Na), assessed
671 using the τ mass transport model and molar element ratios, suggests an order of susceptibility of
672 Na ≈ Ca ≈ Sr > Mg > Ba > Be. This order of mobility during weathering, with the exception of
673 Mg, is consistent with the data from work of on the river sediments and water of the drainage
674 basins in the Deccan Traps (Das et al., 2005; Das and Krishnaswami, 2006, 2007), as discussed
675 further below.

676 *6.1.1 Na, Ca, Sr*

677 The behaviour of Ca, Na, and Sr are strongly linked in the profile. For example, the Sr
678 concentration is highly correlated with the CIA (r^2=0.977) and the $\tau_{Nb,Sr}$ values with $\tau_{Nb,Ca}$
679 (r^2=0.973). These elements exhibit the greatest net depletion based on the $\tau_{Nb,j}$ values (Na: 100%,
680 assuming a concentration of 0 for analyses below the detection limit of the XRF; Ca: 90%; Sr:
681 87%). They are hosted predominantly in plagioclase, which is highly susceptible to chemical
682 weathering. The average molar Ca/Na ratio of the least-weathered basalt samples (CIA ≤ 40:
683 ChQB12, ChQB9b-d) in the Chhindwara profile is 2.26 ± 0.06 (n=4), which is near the average
684 of the Poladpur and Ambenali formations (2.45-2.53; Subbarao et al., 2000; Widdowson et al.,
685 2000). The Ca/Na is relatively constant in the remainder of the profile, with two exceptions.
686 First, slightly lower Ca/Na ratios are present in three samples at the base of the upper flow
687 (ChQB3-ChQB5; Ca/Na: 1.60-1.75), possibly indicating enhanced Ca removal. Second, the
688 Ca/Na ratios approach infinity for the samples in which Na is below the detection limit of the
689 XRF. This observation, coupled with the near constant molar Ca/Na ratios in Deccan river

690 sediments (Das and Krishnaswami, 2007) and river waters (Das et al., 2005) suggests that Ca and
691 Na are removed congruently from the Deccan basalt during chemical weathering.

692 *6.1.2 Mg*

693 A strong depletion of Mg follows the other alkaline earth elements at the base of the upper flow,
694 as indicated by the correlation of $\tau_{Nb,Mg}$ with $\tau_{Nb,Ca}$ (r^2=0.952) and the relatively invariable molar
695 Ca/Mg ratio. The latter ratio is similar to the least-weathered basalt samples (constant at 1.37 ±
696 0.03, n=4) and the range exhibited by unweathered Deccan basalts (Subbarao et al., 2000;
697 Widdowson et al., 2000). The change in weathering behaviour of Mg in the lower flow (Section
698 5.2.2) is expressed by lower Ca/Mg ratios, which range from 0.29 to 0.72. Although the spread in
699 $\tau_{Nb,Mg}$ values in the lower flow is small (65-73% depletion), the minor variations appear to be
700 anti-correlated with Ca, Na, and Sr loss. This change in Mg weathering behaviour is unlikely to
701 be important to the overall flux of Mg to the hydrosphere from the weathering of the Deccan
702 basalt province. Near-constant Mg/Sr and Ca/Mg ratios of the Deccan river sediments suggest a
703 similar and congruent weathering behaviour of Mg to these other alkaline earth elements (Das
704 and Krishnaswami, 2007). However, the river water data do exhibit notable scatter in the Ca/Mg
705 ratio (Das et al., 2005) and this may indicate that preferential leaching of Ca relative to Mg is
706 important locally, consistent with the observations of Mg in the lower flow of the Chhindwara
707 profile.

708 *6.1.3 Ba*

709 The $\tau_{Nb,Ba}$ values, although reaching up to 68% depletion, indicate a higher retention for Ba than
710 most other alkaline earth elements and the values are less correlated with the CIA. There are
711 some areas of local Ba enrichment (~75 %), such as near the soil surface. By comparison, the

712 ionic radius of Ba^{2+} is larger and much closer to that of K^{+}, suggesting a stronger association
713 with pedogenetic phyllosilicates. Although Ba and K are not directly correlated in the
714 Chhindwara profile, they are in the river sediments of the Deccan Traps (Das and Krishnaswami,
715 2007), indicating a broadly similar retention in sediments derived from the Deccan Traps.

716 Barium has long been known to exhibit a different weathering behaviour than the other, more
717 mobile alkaline earth elements (e.g., Nesbitt et al., 1980; Buggle et al., 2011). It is often
718 contrasted with Sr since the Ba^{2+} and Sr^{2+} ionic radii differ by roughly 12-13% in the same
719 coordination, leading to the disparity in their mobility. Accordingly, the Ba/Sr ratio has been
720 applied as an index of the degree of alkaline earth element depletion or leaching during
721 hydrolysis (e.g., Retallack, 1994; Gallet et al., 1996). The Ambenali and Poladpur formations
722 have average molar Ba/Sr ratios that range from 0.24 to 0.38 (Widdowson et al., 2000). The
723 Ba/Sr ratio of the Chhindwara profile evolves from a similar ratio of ~0.3 in the least-weathered
724 samples to a maximum of 0.7 (if the horizons of Ba enrichment are excluded). Collectively, the
725 Ba geochemistry of Deccan Traps river waters and sediments confirm its less mobile behaviour
726 during basalt weathering. The mean ratios of Ba to other alkaline earth elements (Sr, Mg, Ca) in
727 Deccan rivers are typically 2-3 times lower than the Deccan basalt (Das and Krishnaswami,
728 2006) and the river sediment Ba/Sr ratios are highly variable, ranging from 0.3 to 3.2, with a
729 mean value of 1.1 (Das and Krishnaswami, 2007). The sediment samples with the highest Ba/Sr
730 appear to be heavily influenced by the sediments of the Krishna tributaries, which may have a
731 greater input of lateritised products that experienced greater degrees of leaching.

732 *6.1.4 Be*

733 In the Chhindwara weathering profile, the $\tau_{Nb,Be}$ values are the highest of all of the alkaline earth
734 elements, suggesting it is the least mobile of the group. The best correlation of $\tau_{Nb,Be}$ is found
735 with $\tau_{Nb,Ba}$ and $\tau_{Nb,Li}$. Despite its slight depletion, it appears that the small ionic radius of Be^{2+}
736 results in a less mobile behaviour, possibly due to the greater potential of the cation to form
737 insoluble hydrolysates.

738 **6.2 Alkali elements (+Thallium)**

739 The alkali elements, with their lower ionic potential compared to the alkaline earths, are more
740 strongly associated with the phyllosilicates, substituting into interlayer sites or adsorbing to clay
741 mineral surfaces. Despite the high solubility of many of the alkali elements, this factor tends to
742 lead to a lower mobility during weathering (Nesbitt et al., 1980). This is evident by the $\tau_{Nb,j}$
743 values for the alkali elements (see Figure 9 for values and trends with depth), which exhibit
744 minimal to no positive or negative correlation with the CIA, indicating a strong decoupling from
745 the mobile alkaline earth elements. When the $\tau_{Nb,j}$ values of several alkali elements are plotted
746 against each other, two separate correlations normally result, suggesting the mass balance
747 calculations are more greatly influenced by the different parent flow chemistry. Included with the
748 alkali elements is thallium (Tl) due to its similar geochemical properties, namely a commonly
749 monovalent charge and similar ionic radius (Shannon, 1976). The behaviour of Li is largely
750 decoupled from the remaining alkali elements and is discussed separately in Section 6.2.1.

751 Overall, the alkali elements closest in ionic radius exhibit the most similar behaviour and the
752 correlations between the element concentrations and mass balance values decrease. For example,
753 strong correlations exist between $\tau_{Nb,K}$ and $\tau_{Nb,Rb}$ within the separate flows in the Chhindwara
754 profile (r^2=0.832 in the upper and r^2=0.939 in the lower). Using similar relative relationships, the

755 behaviour of Cs is most closely associated with Rb, and the behaviour of Tl is closely related
756 with Rb. In the latter case, a similar weathering behaviour can also be inferred from the strong
757 correlation of these elements in alluvial sediment (Kamber et al., 2005).

758 *6.2.1 Li*

759 A more significant anti-correlation, similar to the alkaline earth elements, is found between the
760 $\tau_{Nb,Li}$ values and the CIA (Figure 10). As an expected consequence, the $\tau_{Nb,Li}$ values correlate
761 better with those of Na, Ca, and Sr and less with the other alkali elements (i.e., Rb, K, Cs). The
762 behaviour of lithium during continental weathering is reasonably well understood and the subject
763 of more detailed focus due to stable isotope fractionation during pedogenesis (Huh et al., 2001;
764 Rudnick et al., 2004). In general, Li is expected to be more mobile during weathering than the
765 other alkali elements (excluding Na), but has a stronger affinity for phyllosilicates, likely as a
766 result of coupled substitution with Mg^{2+} for Al^{3+} in the octahedral sites (Ronov et al., 1970;
767 Anderson et al., 1989; Huh et al., 2004).

768 *6.2.2 Alkali element enrichment*

769 Withheld from the previous discussion were three samples from the lower flow of the
770 Chhindwara profile that appear to have experienced K addition (Section 5.1.3). Based on the $\tau_{Nb,j}$
771 values, this K enrichment is up to 400 % of the parent rock concentration. This enrichment
772 extends to the other elements in the alkali group (Figure 9), with the most extreme enrichment
773 exhibited by Cs (~1500 %), followed by Rb (~1000 %) and Tl (~110 %). In many Phanerozoic to
774 modern weathering profiles, K enrichment is attributed to preferential uptake in plants and/or the
775 addition of an allochthonous, K-rich material such as aeolian dust (Sheldon, 2003).

776 Stratigraphically, these samples constitute the vesicular and brecciated flow top. Accordingly,
777 input of allochthonous material (dust or sediment) to the lava flow during or after emplacement
778 is a likely explanation for the enrichment (e.g., Ghosh et al., 2006). Since the alkali elements are
779 depleted in the mantle source of most basalt and highly enriched in the continental crust, only
780 minor degrees of allochthonous addition could generate significant chemical enrichments.
781 Further work, such as high-precision Nd isotope analysis could substantiate this hypothesis
782 (Mason et al., 2000). The alternative explanation, biological enrichment of K (e.g., Sheldon,
783 2003), remains less favourable since the enrichment extends to the other alkali elements and it is
784 localised to only the flow top zone.

785

786 **7. RESULTS AND DISCUSSION – PART III**

787 **Behaviour of the rare earth elements during basalt weathering**

788 The CI-chondrite normalised REE patterns of the three least-weathered samples from the Bidar
789 (BB1) and Chhindwara (ChQB12 and ChQB9d) weathering profiles (Table 4) are nearly
790 identical, differing only in absolute abundance. This justifies their use as parent rock values for
791 normalising the progressively more weathered samples (Figure 11). This normalisation most
792 readily exposes REE mobility (e.g., Laveuf et al., 2008). The REE are known to be variably
793 mobile during weathering and fractionate during pedogenesis (e.g., Nesbitt, 1979; Duddy, 1980;
794 Braun et al., 1993; Cotten et al., 1995; Laveuf and Cornu, 2009 and the references therein;
795 Sanematsu et al., 2011), but there is still little consensus regarding the details of the behaviour.

796 *7.1 Overall REE behaviour*

797 Fractionation of the REE in the Chhindwara and Bidar weathering profiles is evident in the
798 change in abundance and slope of the normalised REE patterns in Figure 11. In most of the
799 Chhindwara samples, the REE are enriched relative to the least-weathered sample (ChQB12) and
800 that retention follows the general order of LREE>MREE>HREE during the weathering
801 progression. This observation is consistent with previous studies regarding the mobility of the
802 REE during pedogenesis (e.g., Laveuf and Cornu, 2009 and the references therein) whereby the
803 LREE are less readily fluid-complexed than the HREE and become enriched in weathering
804 products such as the phyllosilicates (e.g., Nesbitt, 1979; Mongelli, 1993).

805 The REE abundance of the samples in the Bidar laterite profile changes more significantly
806 relative to the parent rock (Figure 11c). A more pronounced depletion is evident within the
807 highly lateritised (upper 10 m) zone of the profile. If the REE are predominantly associated with
808 clays in the early-forming weathering residue, the advanced stages of Si loss during lateritisation
809 appears to release them from the profile. A higher retention of the LREE, however, is still
810 present in the lateritised samples (Figure 11c). The MREE are more depleted than the LREE and
811 HREE during the advanced stages of weathering. As an exception to the above samples, BB3 has
812 a highly anomalous REE pattern and abundance. It is significantly enriched relative to the parent
813 basalt and has an extremely high HREE/LREE slope. This sample may represent a horizon in
814 which REE (and preferentially the HREE) leached from higher in the profile and accumulated at
815 a site of contrasting pH and/or decreased permeability (e.g., Braun et al., 1998; Patino et al.,
816 2003; Viers and Wasserburg, 2004; Kamgang Kabeyene Beyala et al., 2009), such as near the
817 saprolite-protolith boundary. When studying deep, highly advanced weathering profiles,
818 however, the addition of allochthonous material (e.g., dust) can also potentially influence the
819 chemistry of the profile during long surface exposure times (e.g., Kisakürek et al., 2004;

820 Wimpenny et al., 2007). Further, constraining the influence of dust addition to the REE
821 chemistry of the Bidar laterite is also difficult without knowledge of the chronology of lava
822 stacking and dust composition at the time of accumulation.

823 *7.2 Sm/Nd fractionation*

824 In addition to the obvious changes in the LREE/HREE abundance during pedogenesis,
825 fractionations between some of the closely spaced REE are also detectable, as exemplified by the
826 Sm/Nd ratio. If both flows are considered together, a decrease in Sm/Nd correlates with
827 increasing weathering intensity (r^2=0.813; Figure 12). The parent basalt Sm/Nd ratio of the upper
828 and lower flows appears to have differed slightly, which complicates the superimposed effects
829 resulting from chemical weathering.

830 These observations suggest that Sm/Nd and, consequently, Nd isotope systematics of altered
831 basalt and derived sediments are sensitive to pedogenetic fractionation. This would not alter the
832 Nd isotope composition of modern profiles or sediments, but fractionation in Sm/Nd would
833 manifest as variations in the Nd isotope composition in ancient weathering profiles. In this sense,
834 the more weathered material would be less radiogenic as a result of the lower Sm/Nd generated
835 during LREE enrichment. This has been exploited to crudely date the age of paleosols since an
836 isochron develops that is proportional to the age of pedogenesis (e.g., Stafford, 2007; Frei and
837 Polat, 2013). Using the Chhindwara profile as an example, the extent of Sm/Nd fractionation in
838 the upper flow would translate to a one ε_{Nd} unit difference over a billion years. Note that this
839 calculation assumes that all of the change in the $^{147}Sm/^{144}Nd$ is generated from pedogenesis
840 (highest ratio in the parent basalt and the lowest in the most weathered material), the initial

841 parent rock $^{143}Nd/^{144}Nd$ is constant, and that the isotope system remains closed after pedogenetic
842 fractionation.

843 These findings contradict the conclusions of Nesbitt and Markovics (1997), where changes in
844 Sm/Nd were undetectable in weathered granodiorite. Therefore, more extreme LREE
845 fractionation may occur during basaltic weathering by comparison to more felsic and/or coarser
846 grained rocks. At present, it is difficult to attribute this to a property of the parent rock (e.g.,
847 grain size, bulk composition, mineralogy), differences in the pedogenetic mineralogy, or the
848 weathering environment (e.g., drainage, organic matter). Regardless, given the high erosion rates
849 of basaltic terrain and their greater abundance on the early Earth, this is an important
850 consideration for global weathering fluxes. Further, it seems that the Sm/Nd (or La/Ce) ratio may
851 not always be an ideal provenance indicator, as advocated, for instance, by Sheldon and Tabor
852 (2009). Tests of immobility should be made, if possible, prior to provenance interpretation.

853 *7.3 Europium anomaly (Eu/Eu*)*

854 Europium is the only lanthanide that commonly occurs in a divalent oxidation state and whose
855 behaviour is strongly influenced by plagioclase. This results in the potential for Eu to fractionate
856 from the other lanthanides during weathering, since plagioclase is one of the most susceptible
857 minerals to chemical dissolution. Fractionation of Eu can be tracked using the Eu anomaly
858 [$Eu/Eu^* = Eu_n/(Sm_n \times Gd_n)^{1/2}$]. In the following discussion, the Eu/Eu* values are calculated using
859 normalisation to the parent rock sample of the profile in question. Qualitatively, it is apparent
860 that nearly all of the samples within both weathering profiles have a negative Eu anomaly
861 (Figure 11).

862 The Eu/Eu* values in the Chhindwara profile decrease from 1 to ~0.75. Importantly, this
863 variation in the Eu/Eu* value is inversely correlated with the CIA (Figure 13a). During the
864 earliest stages of weathering recorded within the upper flow of the Chhindwara profile (CIA: 35-
865 70), there is only a subtle change in the Eu anomaly (to as low as 0.90). Within the lower flow of
866 the Chhindwara profile (CIA: 70-80), the slope of the CIA vs. Eu/Eu* anti-correlation steepens
867 and Eu/Eu* reaches its lowest values. The same inverse correlation of the Eu/Eu* value with the
868 CIA in the Chhindwara profile also exists with Sr concentration and the Rb/Sr ratio (Figure 13b),
869 including the same inflection point at the transition from the upper to lower flow. Although these
870 observations could indicate more aggressive Eu loss at higher degrees of weathering intensity in
871 the lower flow, the minor variation in the primary chemistry of the two flows is probably the
872 cause for the apparently different slope. Regardless, these observations confirm a strong
873 relationship between Eu loss and plagioclase weathering. Similar reports of a declining negative
874 Eu anomaly as a function of weathering intensity have been made previously (e.g., Condie et al.,
875 1995; Huang and Gong, 2001; Ma et al., 2011). In the study of Ma et al. (2011), pore waters
876 within the local weathering residuum possessed a positive Eu anomaly. Lawrence et al. (2006)
877 noted that when river waters were normalised to the composition of their catchment geology,
878 significant variation in the Eu anomaly remained that suggested a more complicated and possibly
879 mineral-specific weathering contribution to the waters (such as preferential plagioclase
880 dissolution).

881 In the Bidar laterite samples, the Eu/Eu* values are essentially constant between 0.85 and 0.90,
882 indicating that a similar, albeit less pronounced, depletion of Eu has occurred relative to the
883 parent sample (BB1). The Eu/Eu* value, however, does not change as a function of the
884 weathering intensity in the Bidar samples (i.e., there is no obvious correlation between the IOL

and Eu/Eu*). This confirms that the major loss of Eu occurs during the earlier stages of weathering. By the time all plagioclase has been removed from the weathering profile, the Eu/Eu* variability ceases and the remaining Eu changes only as a function of the processes affecting the remaining trivalent lanthanides. The possibility needs to be considered that Eu/Eu* could also have been affected by dust introduction during weathering exposure.

7.4 Ce anomaly (Ce/Ce)*

Cerium can track redox-related transformations during pedogenesis in modern and ancient weathering profiles as a result of the potential oxidation of Ce^{3+} to Ce^{4+} (e.g., Middelburg et al., 1988; Braun et al., 1990; Mongelli, 1993; Gallet et al., 1996; Murakami et al., 2001; Patino et al., 2003). A positive Ce anomaly [$Ce/Ce^*=Ce_n/(La_n \times Pr_n)^{1/2}$] develops at sites of Ce enrichment, although there are often cases of weathered samples displaying distinct negative Ce anomalies, presumably generated by the cycling of REE away from areas of Ce enrichment (e.g., Nesbitt, 1979; Marsh, 1991; Fodor et al., 1992; Cotten et al., 1995). It is evident from the REY plots of the weathered Deccan basalt (Figure 11) that Ce is fractionated to varying degrees (relative to La and Pr) in nearly all samples, confirming its decoupling from the other LREE.

The Ce concentration increases during the incipient to intermediate weathering of the Chhindwara basalt along with the other LREE. There is, however, no obvious correlation between the Ce/Ce* value and the degree of weathering and several samples in the upper flow have negative anomalies. The presence of negative and positive Ce anomalies indicates that Ce oxidation is probably occurring at a smaller scale in the weathering front (e.g., Taunton et al., 2000). By contrast, within the lower and more highly weathered flow (CIA > 70), more samples have positive and higher Ce anomalies.

907 The Bidar laterite profile has much more extreme variation in Ce/Ce* with values ranging from
908 0.27 to 6.71. The Ce anomaly does not have any obvious correlations with the IOL, although the
909 two highest Ce/Ce* values (BB7: 4.14 and BB9: 6.71) are within the upper, most highly
910 lateritised portion of the weathering profile. This is consistent with the implied importance of
911 specific oxides and secondary minerals (e.g., florencite; Sanematsua et al., 2011) in the
912 fractionation of the REE. The REE-enriched sample deep in the profile (BB3), has the most
913 negative Ce anomaly (0.27), indicating that the lanthanides transported from above were likely
914 leached in the presence of Mn oxides from higher in the profile.

915

916 **8. CONCLUSIONS**

917 In this study, two weathering profiles located in the Deccan Traps, India, were studied to better
918 quantify and understand different stages of basalt alteration. In basaltic weathering
919 environments, lava flow morphology and texture (e.g., flow banding and vesicularity) are
920 dominant controls on the penetration of weathering fluids and fluid-rock interaction.
921 Mineralogical differences, such as the presence of zeolites, may also affect chemical weathering
922 progression. Weathering profiles can develop across several basalt flows and some primary
923 chemical variations from the original flows may survive overprinting by pedogenesis (e.g.,
924 HFSE ratios). From a geochemical perspective, this influences the precision of alteration mass
925 balance calculations, especially where unweathered parent material is not available from
926 different flows.

927 In order to better understand mafic substrate alteration, a new chemical weathering index, the
928 mafic index of alteration (MIA), is proposed. The dichotomous, redox-related behaviour of Fe is

929 factored into two separate MIA equations suitable for reducing [$MIA_{(R)}$] or oxidising [$MIA_{(O)}$]
930 environments. The quantitative MIA value can be used in combination with ternary plots in the
931 Al–Fe–Mg–Ca–Na–K system that display the proportional chemical changes. Like the majority
932 of currently established weathering indices, the MIA is most suitable for understanding the early
933 to intermediate stages of chemical weathering ('kaolinitisation'). Obtaining a quantitative handle
934 on advanced chemical weathering requires a different approach. We propose using the index of
935 lateritisation (IOL) as a quantitative expression of the Si–Al–Fe (SAF) ternary plot (Schellmann,
936 1981, 1982, 1986). Plotting chemical weathering indices against LOI values can provide
937 additional insight into pedogenetic mineral transformations.

938 Chemical weathering studies should always start with the major element composition of the
939 weathering profile prior to trace element or isotopic analysis. When used in combination,
940 weathering indices and high-precision trace element analysis can provide insight into which
941 stages of alteration the trace element loss or retention are associated with. In the present study,
942 the focus is on the alkali, alkaline earth, and rare earth elements of the basaltic weathering
943 profiles. The main observations and conclusions presented are:

944 - The alkali and alkaline earth element geochemistry in the Chhindwara profile conforms
945 predominantly to the expected weathering behaviour. The alkaline earth elements (+Na)
946 exhibit an order of depletion of Na ≈ Ca ≈ Sr > Mg > Ba > Be. By contrast, the alkali
947 elements exhibit a greater retention in the altered substrate. Notably, Tl appears to
948 behave most closely to Rb and Li exhibits the greatest mobility of the alkali elements.
949 - Alkali element enrichment (Cs, Tl, Rb, K) at the paleo-flow top of the Chhindwara
950 profile is best explained by the allochthonous addition of dust to the profile. The results
951 show that the enrichment in K reported in other studies may similarly be accompanied by

the other alkali elements. This may help constrain the mechanism of enrichment (e.g., metasomatism, plant uptake, dust).

- Rare earth element fractionation occurs during weathering of the Deccan basalt whereby the enrichment of the LREE is greater than the MREE and HREE in the weathering residue. Significant pedogenetic fractionation of the closely spaced LREE is also evident from variation in the Sm/Nd ratio. Consequently, this indicates that REE ratios should be treated with caution when used for assessing the provenance of weathered materials. Fractionation of Sm/Nd can manifest as a varying Nd isotope composition over time.
- The preferential loss of Eu, measured with the Eu anomaly (Eu/Eu*) is highly correlated with Sr, Ca, and Na loss from plagioclase. Following the complete weathering of plagioclase, the Eu/Eu* does not appear to change further as a function of weathering intensity.
- Cerium is fractionated from the trivalent lanthanides during pedogenesis but there is a lack of correlation of Ce/Ce* with any of the weathering indices, consistent with fractionation being controlled by pedogenetic minerals that are not contributing to the calculation of the weathering indices.

The results presented here are relevant to ancient paleosol research and may be useful for studying Martian substrate alteration.

ACKNOWLEDGEMENTS

973 The analytical work for this study was funded by an NSERC Discovery grant to BSK. The
974 fieldwork of MW was supported by travel grants received from The Mineralogical Society, UK,
975 and The Geological Society of London. Financial support to MGB was provided by an NSERC
976 Canadian Graduate Scholarship at Laurentian University and an Ussher Fellowship at Trinity
977 College Dublin. D. Klinck is acknowledged for contributions to the study as part of his BSc
978 thesis at Laurentian University. The authors would like to acknowledge A. Gladu for analytical
979 assistance and C. Kamber for drafting of the Chhindwara maps and profile sketch. Insightful
980 comments by two anonymous reviewers improved the content and clarity of the manuscript.

WORKS CITED

Aleva, G.J.J., 1994. Laterites: Concepts, Geology, Morphology and Chemistry. ISRIC, Wageningen.

Anderson, M.A., Bertsch, P.M., Miller, W.P., 1989. Exchange and apparent fixation of lithium in selected soils and clay-minerals. Soil Science 148, 46-52.

Anderson, S.P., Dietrich, W.E., Brimhall, G.H., Jr., 2002. Weathering profiles, mass-balance analysis, and rates of solute loss: Linkages between weathering and erosion. Geological Society of America Bulletin 114, 1143-1158.

Babechuk, M.G., Kamber, B.S., Greig, A., Canil, D., Kodolányi, J., 2010. The behaviour of tungsten during mantle melting revisited with implications for planetary differentiation time scales. Geochimica et Cosmochimica Acta 74, 1448-1470.

Beauvais, A., 1999. Geochemical balance of lateritization processes and climatic signatures in weathering profiles overlain by ferricretes in Central Africa. Geochimica et Cosmochimica Acta 63, 3939-3957.

Beck, R.A., Burbank, D.W., Sercombe, W.J., Riley, G.W., Barndt, J.K., Berry, J.R., Afzal, J., Khan, A.M., Jurgen, H., Metje, J., Cheema, A., Shafique, N.A., Lawrence, R.D., Khan, M.A., 1995. Stratigraphic evidence for an early collision between northwest India and Asia. Nature 373, 55-58.

Bhattacharyya, T., Pal, D.K., Srivastava, P., 1999. Role of zeolites in persistence of high altitude ferruginous Alfisols of the humid tropical Western Ghats, India. Geoderma 90, 263-276.

1001 Borger, H., Widdowson, M., 2001. Indian laterites, and lateritious residues of southern Germany:
1002 a petrographic, mineralogical, and geochemical comparison. Zeitschrift für
1003 Geomorphologie, NF 25, 177-200.

1004 Bourman, R.P., 1993. Perennial problems in the study of laterite: a review. Australian Journal of
1005 Earth Sciences 40, 387-401.

1006 Bourman, R.P., Ollier, C.D., 2002. A critique of the Schellmann definition and classification of
1007 'laterite'. Catena 47, 117-131.

1008 Bourman, R.P., Ollier, C.D., 2003. Reply to the discussion of "A critique of the Schellmann
1009 definition and classification of laterite" by R.P. Bourman and C.D. Ollier (Catena 47,
1010 117-131). Catena 52, 81-83.

1011 Braun, J.-J., Pagel, M., Muller, J.P., Bilong, P., Michard, A., Guillet, B., 1990. Cerium anomalies
1012 in lateritic profiles. Geochim. Cosmochim. Acta 54, 781-795.

1013 Braun, J.-J., Pagel, M., Herbillon, A., Rosin, C., 1993. Mobilization and redistribution of REEs
1014 and thorium in a syenitic lateritic profile: A mass balance study. Geochimica et
1015 Cosmochimica Acta 57, 4419-4434.

1016 Braun, J.-J., Viers, J., Dupré, B., Polve, M., Ndam, J., Muller, J.-P., 1998. Solid/liquid REE
1017 fractionation in the lateritic system of Goyoum, East Cameroon: the implication for
1018 present dynamics of the soil covers of the humid tropical regions. Geochimica et
1019 Cosmochimica Acta 62, 273-299.

1020 Brimhall, G.H., Dietrich, W.E., 1987. Constitutive mass balance relations between chemical
1021 composition, volume, density, porosity, and strain in metasomatic hydrochemical

systems: Results on weathering and pedogenesis. Geochimica et Cosmochimica Acta 31, 567-587.

Buggle, B., Glaser, B., Hambach, U., Gerasimenko, N., Marković, S., 2011. An evaluation of geochemical weathering indices in loess-paleosol studies. Quaternary International 240, 12-21.

Chenet, A.L., Quidelleur, X., Fluteau, F., Courtillot, V., Bajpai, S., 2007. $^{40}K—^{40}Ar$ dating of the Main Deccan large igneous province: further evidence of KTB age and short duration. Earth and Planetary Science Letters 263, 1-15.

Chesworth, W., Dejou, J., Larroque, P., 1981. The weathering of basalt and relative mobilities of the major elements at Belbex, France. Geochimica et Cosmochimica Acta 45, 1235-1243.

Clift, P., Gaedicke, C., Edwards, R., Lee, J.L., Hildebrand, P., Amjad, S., White, R.S., Schlüter, H.-U., 2002. The stratigraphic evolution of the Indus Fan and the history of sedimentation in the Arabian Sea. Marine Geophysical Researches 23, 223-245.

Condie, K.C., Dengate, J., Cullers, R.L., 1995. Behaviour of rare earth elements in a paleoweathering profile on graniodiorite in the Front Range, Colorado, USA. Geochimica et Cosmochimica Acta 59, 279-294.

Cotten, J., Le Dez, A., Bau, M., Caroff, M., Maury, R.C., Dulski, P., Fourcade, S., Bohn, M., Brousse, R., 1995. Origin of anomalous rare-earth element and yttrium enrichments in subaerially exposed basalts: evidence from French Polynesia. Chemical Geology 119, 115-138.

1042 Craig, D.C., Loughnan, F.C., 1964. Chemical and mineralogical transformations accompanying
1043 the weathering of basic volcanic rocks of New South Wales. Australian Journal of Soil
1044 Research 2, 218-234.

1045 Das, A., Krishnaswami, S., Sarin, M.M., Pande, K., 2005. Chemical weathering in the Krishna
1046 Basin and Western Ghats of the Deccan Traps, India: Rates of basalt weathering and their
1047 controls. Geochimica et Cosmochimica Acta 69, 2067-2084.

1048 Das, A., Krishnaswami, S., 2006. Barium in Deccan basalt rivers: Its abundance, relative
1049 mobility and flux. Aquatic Chemistry 12, 221-238.

1050 Das, A., Krishnaswami, S., 2007. Elemental geochemistry of river sediments from the Deccan
1051 Traps, India: Implications to sources of elements and their mobility during basalt–water
1052 interaction. Chemical Geology 242, 232-254.

1053 Dessert, C., Dupré, B., François, L.M., Schott, J., Gaillardet, J., Chakrapani, G., Bajpai, S., 2001.
1054 Erosion of Deccan Traps determined by river geochemistry: impact on the global climate
1055 and the $^{87}Sr/^{86}Sr$ ratio of seawater. Earth and Planetary Science Letters 188, 459-474.

1056 Driese, S.G., 2004. Pedogenic translocation of Fe in modern and ancient vertisols and
1057 implications for interpretations of the Hekpoort paleosol (2.25 Ga). The Journal of
1058 Geology 112, 543-560.

1059 Duddy, L.R., 1980. Redistribution and fractionation of rare-earth and other elements in a
1060 weathering profile. Chemical Geology 30, 363-381.

1061 Duncan, R.A., Pyle, D.G., 1988. Rapid eruption of the Deccan flood basalts at the
1062 Cretaceous/Tertiary boundary. Nature 333, 841-843.

1063 Duzgoren-Aydin, N.S., Aydin, A., Malpas, J., 2002. Re-assessment of chemical weathering
1064 indices: case study on pyroclastic rocks of Hong Kong. Engineering Geology 63, 99-119.

1065 Duzgoren-Aydin, N.S., Aydin, A., 2003. Chemical heterogeneities of weathered igneous
1066 profiles: implications for chemical indices. Environmental & Engineering Geoscience 9,
1067 363-377.

1068 Eggins, S.M., Woodhead, J.D., Kinsley, L.P.J., Mortimer, G.E., Sylvester, P., McCulloch, M.T.,
1069 Hergt, J.M., Handler, M.R., 1997. A simple method for the precise determination of ≥ 40
1070 trace elements in geological samples by ICPMS using enriched isotope internal
1071 standardisation. Chemical Geology 134, 311-326.

1072 Eggleton, R.A., Foudoulis, C., Varkevisser, D., 1987. Weathering of basalt: changes in rock
1073 chemistry and mineralogy. Clays and Clay Minerals 35, 161-169.

1074 Fedo, C.M., Nesbitt, H.W., Young, G.M., 1995. Unravelling the effects of potassium
1075 metasomatism in sedimentary rocks and paleosols, with implications for paleoweathering
1076 conditions and provenance. Geology 23, 921-924.

1077 Fodor, R.V., Frey, F.A., Bauer, G.R., Clague, D.A., 1992. Ages, rare-earth element enrichment,
1078 and petrogenesis of tholeiitic and alkalic basalts from Kahoolawe Island, Hawaii.
1079 Contributions to Mineralogy and Petrology 110, 442-462.

1080 Frei, R., Polat, A., 2013. Chromium isotope fractionation during oxidative weathering –
1081 implications from the study of a Paleoproterozoic (ca. 1.9 Ga) paleosol, Schreiber Beach,
1082 Ontario, Canada. Precambrian Research 224, 434-453.

1083 Gaillardet, J., Dupré, B., Louvat, P., Allègre, C.J., 1999. Global silicate weathering and CO2
1084 consumption rates deduced from the chemistry of large rivers. Chemical Geology 159, 3-
1085 30.

1086 Gallet, Y., Weeks, R., Vandamme, D., Courtillot, V., 1989. Duration of Deccan trap volcanism:
1087 a statistical approach. Earth and Planetary Science Letters 93, 273-282.

1088 Gallet, S., Jahn, B., Torii, M., 1996. Geochemical characterization of the Luochuan loess-
1089 paleosol sequence, China, and paleoclimatic implications. Chemical Geology 133, 67-88.

1090 Ghosh, P., Sayyed, M.R.G., Islam, R., Hundekari, S.M., 2006. Inter-basaltic clay (bole bed)
1091 horizons from Deccan traps of India: implications for paleo-weathering and paleo-climate
1092 during Deccan volcanism. Palaeogeography, Palaeoclimatology, Palaeoecology 242, 90-
1093 109.

1094 Harnois, L., 1988. The CIW index: a new chemical index of weathering. Sedimentary Geology
1095 55, 319-322.

1096 Hausrath, E.M., Navarre-Sitchler, A.K., Sak, P.B., Williams, J.Z., Brantley, S.L., 2011. Soil
1097 profiles as indicators of mineral weathering rates and organic interactions for a
1098 Pennsylvania diabase. Chemical Geology 290, 89-100.

1099 Hill, I.G., Worden, R.H., Meighan, I.G., 2000. Geochemical evolution of a paleolaterite: the
1100 Interbasaltic Formation, Northern Ireland. Chemical Geology 166, 65-84.

1101 Hofmann, C., Feraud, G., Courtillot, V., 2000. $^{40}Ar/^{39}Ar$ dating of mineral separates and whole
1102 rocks from the Western Ghats lava pile: further constraints on duration and age of the
1103 Deccan traps. Earth and Planetary Science Letters, 180, 13– 27.

1104 Hooper, P., Widdowson, M., Kelley, S., 2010. Tectonic setting and timing of the final Deccan
1105 flood basalt eruptions. Geology 38, 839-842.

1106 Huang, C., Gong, Z., 2001. Geochemical implication of rare earth elements in process of soil
1107 development. Journal of Rare Earths 19, 57-62.

1108 Huh, Y., Chan, L.H., Edmond, J.M., 2001. Lithium isotopes as a probe of weathering processes:
1109 Orinoco River. Earth and Planetary Science Letters 194, 189-199.

1110 Huh, Y., Chan, L.H., Chadwick, O.A., 2004. Behaviour of lithium and its isotopes during
1111 weathering of Hawaiian basalt. Geochemistry, Geophysics, Geosystems 5, Q09002.

1112 Kale, V.S., 2002. Fluvial geomorphology of Indian rivers: an overview. Progress in Physical
1113 Geography 26, 400-433.

1114 Kamber, B.S., 2009. Geochemical fingerprinting: 40 years of analytical development and real
1115 world applications. Applied Geochemistry 24, 1074-1086.

1116 Kamber, B.S., Greig, A., Collerson, K.D., 2005. A new estimate for the composition of
1117 weathered young upper continental crust from alluvial sediments, Queensland, Australia.
1118 Geochimica et Cosmochimica Acta 69, 1041-1058.

1119 Kamgang Kabeyene Beyala, V., Onana, V.L., Ndome Effoudou Priso, E., Parisot, J.C., Ekodeck,
1120 G.E., 2009. Behaviour of REE and mass balance calculations in a lateritic profile over
1121 chlorite schists in South Cameroon. Chemie der Erde 69, 61-73.

1122 Karrat, L., Perruchot, A., Macaire, J.-J., 1998. Weathering of a Quaternary glass-rich basalt in
1123 Bakrit, Middle Atlas Mountains, Morocco. Comparison with a glass-poor basalt.
1124 Geodinamica Acta 11, 205-215.

1125 Kerrick, D.M., Caldeira, K., 1993. Paleoatmospheric consequences of CO_2 released during Early
1126 Cenozoic regional metamorphism in the Tethyan Orogen. Chemical Geology 108, 201-
1127 230.

1128 Kisakürek, B., Widdowson, M., James, R.H., 2004. Behaviour of Li isotopes during continental
1129 weathering: the Bidar laterite profile, India. Chemical Geology 212, 27-44.

1130 Kramers, J.D., 2002. Global modelling of continent formation and destruction through geological
1131 time and implications for CO2 drawdown in the Archaean Eon, in: Fowlder, C.M.R.,
1132 Ebinger, C.J., Hawkesworth, C.J. (Eds.), The Early Earth: Physical, Chemical and
1133 Biological Development. Geological Society, London, Special Publications 199, pp. 259-
1134 274.

1135 Kronberg, B.I., Nesbitt, H.W., 1981. Quantification of weathering, soil geochemistry and soil
1136 fertility. Journal of Soil Science 32, 453-459.

1137 Laveuf, C., Cornu, S., Juillot, F., 2008. Rare earth elements as tracers of pedogenetic processes.
1138 C.R. Geoscience 340, 523-532.

1139 Laveuf, C., Cornu, S., 2009. A review on the potentiality of Rare Earth Elements to trace
1140 pedogenetic processes. Geoderma 154, 1-12.

1141 Lawrence, M.G., Greig, A., Collerson, K.D., Kamber, B.S., 2006. Rare earth element and
1142 Yttrium variability in South East Queensland waterways. Aquatic Geochemistry 12, 39-
1143 72.

1144 Liu, X.-M., Rudnick, R.L., McDonough, W.F., Cummings, M.L., 2013. Influence of chemical
1145 weathering on the composition of the continental crust: insights from Li and Nd isotopes

in bauxite profiles developed on Columbia River basalts. Geochimica et Cosmochimica Acta 115, 73-91.

Louvat, P., Allègre, C.J., 1997. Present denudation rates on the island of Réunion determined by river geochemistry: basalt weathering and mass budget between chemical and mechanical erosions. Geochimica et Cosmochimica Acta 61, 3645-3669.

Ma, L., Jin, L., Brantley, S.L., 2011. How mineralogy and slope aspect affect REE release and fractionation during shale weathering in the Susquehanna/Shale Hills Critical Zone Observatory. Chemical Geology 290, 31-49.

Marsh, J.S., 1991. REE fractionation and Ce anomalies in weathered Karoo dolerite. Chemical Geology 90, 189-194.

Marx, S.K., Kamber, B.S., 2010. Trace-element systematics of sediments in the Murray-Darling Basin, Australia: sediment provenance and palaeoclimate implications of fine scale chemical heterogeneity. Applied Geochemistry 25, 1221-1237.

Mason, T.F.D., Widdowson, M., Ellam, R.M., Oxburgh, R., 2000. Isotopic variability of Sr and Nd in lateritic deposits from the Deccan Traps, India: evidence for an input of aeolian material to the laterites. Journal of Conference Abstracts 5, 674-675.

Maynard, J.B., 1992. Chemistry of modern soils as a guide to interpreting Precambrian paleosols. The Journal of Geology 100, 279-289.

Middelburg, J.J., van der Weijden, C.H., Woittiez, J.R.W., 1988. Chemical processes affecting the mobility of major, minor and trace elements during weathering of granitic rocks. Chemical Geology 68, 253-273.

1167 Mitchell, C. and Widdowson, M. 1991. A Geological Map of the Southern Deccan Traps, India.
1168 Journal of the Geological Society of London 148, 495-505.

1169 Mongelli, G., 1993. REE and other trace elements in a granitic weathering profile from “Serre”,
1170 southern Italy. Chemical Geology 103, 17-25.

1171 Murakami, T., Utsunomiya, S., Imazu, Y., Prasad, N., 2001. Direct evidence of late Archean to
1172 early Proterozoic anoxic atmosphere from a product of 2.5 Ga old weathering. Earth and
1173 Planetary Science Letters 184, 523-528.

1174 Navarre-Sitchler, A., Brantley, S., 2007. Basalt weathering across scales. Earth and Planetary
1175 Science Letters 261, 321-334.

1176 Nesbitt, H.W., 1979. Mobility and fractionation of rare earth elements during weathering of a
1177 granodiorite. Nature 279, 206-210.

1178 Nesbitt, H.W., 1992. Diagenesis and metasomatism of weathering profiles, with emphasis on
1179 Precambrian paleosols, in: Martini, I.P., Chesworth, W. (Eds.), Weathering, Soils &
1180 Paleosols, Elsevier, Netherlands, pp. 127-152.

1181 Nesbitt, H.W., Markovics, G., Price, R.C., 1980. Chemical processes affecting alkalis and
1182 alkaline earths during continental weathering. Geochimica et Cosmochimica Acta 44,
1183 1659-1666.

1184 Nesbitt, H.W., Young, G.M., 1982. Early Proterozoic climates and plate motions inferred from
1185 major element chemistry of lutites. Nature 299, 715-717.

1186 Nesbitt, H.W., Young, G.M., 1984. Prediction of some weathering trends of plutonic and
1187 volcanic rocks based on thermodynamic and kinetic considerations. Geochimica et
1188 Cosmochimica Acta 48, 1523-1534.

1189 Nesbitt, H.W., Young, G.M., 1989. Formation and diagenesis of weathering profiles. Journal of
1190 Geology 97, 129-147.

1191 Nesbitt, H.W., Wilson, R.E., 1992. Recent chemical weathering of basalts. American Journal of
1192 Science 292, 740-777.

1193 Nesbitt, H.W., Markovics, G., 1997. Weathering of granodioritic crust, long-term storage of
1194 elements in weathering profiles, and petrogenesis of siliciclastic sediments. Geochimica
1195 et Cosmochimica Acta 61, 1653-1670.

1196 Newbold, T.J., 1844. Notes chiefly geological, across the Peninsula from Masultipatam to Goa,
1197 comprising remarks on the origin of regur and laterite: occurrence of manganese veins in
1198 the latter and on certain traces of aqueous denudation on the surface of southern India. *J.*
1199 *Asiat. Soc. Beng.* 15, 204-213, 224-231, 380-396.

1200 Newbold, T.J., 1846. Summary of the geology of Southern India. VI: Laterite. Journal of the
1201 Royal Asiatic Society of Great Britain & Northern Ireland, 227-240.

1202 Nordt, L.C., Driese, S.D., 2010. New weathering index improves paleorainfall estimates from
1203 Vertisols. Geology 38, 407-410.

1204 Oh, N.-H., Richter, D.D., 2005. Elemental translocations and loss from three highly weathered
1205 soil-bedrock profiles in the southeastern United States. Geoderma 126, 5-25.

1206 Ohta, T., Arai, H., 2007. Statistical empirical index of chemical weathering in igneous rocks: a
1207 new tool for evaluating the degree of weathering. Chemical Geology 240, 280-297.

1208 Ollier, C.D., Galloway, R.W., 1990. The laterite profile, ferricretes and unconformity. Catena 17,
1209 97-109.

1210 Parker, A., 1970. An index of weathering for silicate rocks. Geological Magazine 107, 501-504.

1211 Patino, L.C., Velbel, M.A., Price, J.R., Wade, J.A., 2003. Trace element mobility during
1212 spheroidal weathering of basalts and andesites in Hawaii and Guatemala. Chemical
1213 Geology 202, 343-364.

1214 Price, R.C., Gray, C.M., Wilson, R.E., Frey, F.A., Taylor, S.R., 1991. The effects of weathering
1215 on rare-earth element, Y and Ba abundances in Tertiary basalts from southeastern
1216 Australia. Chemical Geology 93, 245-265.

1217 Prudêncio, M.I., Sequeira Braga, M.A., Paquet, H., Waerenborgh, J.C., Pereira, L.C.J., Gouveia,
1218 M.A., 2002. Clay mineral assemblages in weathered basalt profiles from central and
1219 southern Portugal: climatic significance. Catena 49, 77-89.

1220 Rasmussen, C., Dahlgren, R.A., Southard, R.J., 2010. Basalt weathering and pedogenesis across
1221 an environmental gradient in the southern Cascade Range, California, USA. Geoderma
1222 154, 473-485.

1223 Retallack, G.J., 1994. A pedotype approach to latest Cretaceous and earliest Tertiary paleosols in
1224 eastern Montana. Geological Society of America Bulletin 106, 1377-1397.

1225 Retallack, G.J., 2001. Soils of the past: an introduction to paleopedology, second ed. Blackwell,
1226 Oxford.

1227 Retallack, G.J., 2008. Cool-climate or warm-spike lateritic bauxites at high latitudes? The
1228 Journal of Geology 116, 558-570.

1229 Ronov, A.B., 1970. Geochemistry of lithium in the sedimentary cycle. Geochemistry
1230 International 7, 75-102.

1231 Rudnick, R.L., Tomascak, P.B., Njo, H.B., Gardner, L.R., 2004. Extreme lithium isotopic
1232 fractionation during continental weathering revealed in saprolites from South Carolina.
1233 Chemical Geology 212, 45-57.

1234 Rye, R., Holland, H.D., 1998. Paleosols and the evolution of atmospheric oxygen: a critical
1235 review. American Journal of Science 298, 621-672.

1236 Sayyed, M.R.G., Hundekari, S.M., 2006. Preliminary comparison of ancient bole beds and
1237 modern soils developed upon the Deccan volcanic basalts around Pune (India): potential
1238 for palaeoenvironmental reconstruction. Quaternary International 156-157, 189-199.

1239 Sanematsu, K., Moriyama, T., Sotouky, L., Watanabe, Y., 2011. Mobility of the rare earth
1240 elements in basalt-derived laterite at the Bolaven Plateau, Southern Laos. Resource
1241 Geology 61, 140-158.

1242 Schellmann, W., 1981. Considerations on the definition and classification of laterites, in:
1243 Proceedings of the International Seminar on Lateritisation Processes, IGCP 129 and
1244 IAGC, Trivandrum, India. Oxford and IBH Publishing Company, New Delhi, pp. 1-10.

1245 Schellmann, W., 1982. Eine neue Lateritdefinition. Geologische Jahrbuch D58, 31–47.

1246 Schellmann, W., 1986. A new definition of laterite, in: Banerji, P.K. (Ed.), Lateritisation
1247 Processes. Memoirs of the Geological Survey of India 120, pp. 1-7.

1248 Schellmann, W., 2003. Discussion of "A critique of the Schellmann definition and classification
1249 of laterite" by R.P. Bourman and C.D. Ollier (Catena 47, 117-131). Catena 52, 77-79.

1250 Schwarz, T., 1997. Lateritic bauxite in central Germany and implications for Miocene
1251 palaeoclimate. Palaeogeography, Palaeoclimatology, Palaeoecology 129, 37-50.

1252 Shannon, R.D., 1976. Revised effective ionic radii and systematic studies of interatomic
1253 distances in halides and chalcogenides. Acta Crystallographica A32, 751-767.

1254 Sheldon, N.D., 2003. Pedogenesis and geochemical alteration of the Picture Gorge subgroup,
1255 Columbia River basalt, Oregon. Geological Society of America Bulletin 115, 1377-1387.

1256 Sheldon, N.D., Tabor, N.J., 2009. Quantitative paleoenvironmental and paleoclimatic
1257 reconstruction using paleosols. Earth-Science Reviews 95, 1-52.

1258 Stafford, S.L., 2007. Precambrian paleosols as indicators of paleoenvironments on the early
1259 Earth. Unpublished PhD Thesis, University of Pittsburgh.

1260 Subbarao, K.V., Bodas, M.S., Khadri, S.R.F., Bean, J.E., Kale, V., Widdowson, M., Hooper,
1261 P.R., Walsh, J.N., 2000. Field excursion guide to the western Deccan Basalt Province.
1262 Penrose Deccan 2000, p. 249.

1263 Taunton, A.E., Welch, S.A., Banfield, J.F., 2000. Geomicrobiological controls on light rare earth
1264 element, Y and Ba distributions during granite weathering and soil formation. Journal of
1265 Alloys and Compounds 303-304, 30-36.

1266 Taylor, A.S., Lasaga, A.C., 1999. The role of basalt weathering in the Sr isotope budget of the
1267 oceans. Chemical Geology 161, 199-214.

1268 Viers, J., Wasserburg, G.J., 2004. Behaviour of Sm and Nd in a lateritic soil profile. Geochimica
1269 et Cosmochimica Acta 68, 2043-2054.

1270 Widdowson, M., 1997. Tertiary palaeosurfaces of the SW Deccan, Western India: implications
1271 for passive margin uplift, in: Widdowson, M. (Ed.) Palaeosurfaces: Recognition,
1272 Reconstruction and Palaeoenvironmental Interpretation. Special Publication 120. Bath:
1273 Geological Society Publishing House, pp. 221-248.

1274 Widdowson, M., 2007. Laterite and ferricretes, in: Nash, D.J., McLaren, S.J. (Eds.),
1275 Geochemical Sediments and Landscapes, RGS-IBG Book Series, Blackwell Publishing,
1276 Oxford, pp. 46-94.

1277 Widdowson, M., Cox, K.G., 1996. Uplift and erosional history of the Deccan Traps, India:
1278 evidence from laterites and drainage patterns of the Western Ghats and Konkan Coast.
1279 Earth and Planetary Science Letters 137, 57-69.

1280 Widdowson, M., Gunnell, Y., 1999. Lateritization, geomorphology and geodynamics of a
1281 passive margin: the Konkan and Kanara coastal lowlands of western peninsular India, in:
1282 Thiry, M., Simon-Coinçon, R. (Eds.), Palaeoweathering, Palaeosurfaces and Related
1283 Continental Deposits. Special Publication 27, International Association of
1284 Sedimentologists, Blackwell Publishing, Oxford, pp. 245-274.

1285 Widdowson, M., Pringle, M.S. and Fernandez, O.A. 2000. A post K/T boundary age for
1286 Deccan-type dyke feeder dykes, Goa, India. Journal of Petrology, 41(7), 1177-1194.

Wimpenny, J., Gannoun, A., Burton, K.W., Widdowson, M., James, R.H., Gíslason, S.R., 2007. Rhenium and osmium isotope and elemental behaviour accompanying laterite formation in the Deccan region of India. Earth and Planetary Science Letters 261, 239-258.

Young, G.M., 2013. Secular changes at the Earth's surface: evidence from palaeosols, some sedimentary rocks, and palaeoclimatic perturbations of the Proterozoic Eon. Gondwana Research 24, 453-467.

FIGURE CAPTIONS

****All colour figures are for the web version only**

Figure 1: Illustration showing the transitional relationship from end-member autochthonous to allochthonous duricrusts (i.e., laterite to ferricrete), modified from Widdowson (2007). The Bidar (BB) laterite profile is an autochthonous profile formed from *in situ* weathering.

Figure 2: Simplified geological map showing the extent of the Deccan Volcanic Province (DVP) within peninsular India and the geomorphology of the weathered basaltic terrane. Inset maps show (a) the mesa topography near Chhindwara in the Madya Pradesh district and (b) the more detailed geology of the SE lobe of the DVP, including the extent of the thick laterite that hosts the Bidar profile. DVP geology maps modified from Borger and Widdowson (2001) and Kisakürek et al. (2004).

Figure 3: Geological sketch section of the: a) Bidar laterite (modified from Kisakürek et al., 2004 and Widdowson, 2007) and b) Chhindwara weathering profile. Highlights of the key features in the weathering progression accompany the schematic of each profile. Note the different scales of depth. The Chhindwara weathering profile is developed across two identifiable basalt flows (A – lower flow and B – upper flow). The sample identification and locations are also provided.

Figure 4: Field photographs of the Chhindwara weathering profile. (a) The entirety of the sampled weathering profile exposed in a road side quarry. Note the colour change marking the transition from the upper flow (ChQB) to the lower flow (ChQA). (b) Corestone within the upper flow at a depth of 90 cm from the surface that was divided into four sub-samples (ChQBa-d) for geochemical analysis.

Figure 5: (a) Molar Al_2O_3–CaO*+Na_2O–K_2O (A–CN–K) and (b) mass SiO_2–Al_2O_3–$Fe_2O_{3(T)}$ (SAF) ternary plots illustrating the different degrees of alteration experienced between the Chhindwara (solid squares) and Bidar (solid circles) weathering profiles. The figure symbols for the Bidar and Chhindwara samples and the data compilation are consistent throughout all subsequent figures unless specified otherwise. In both figures, a data compilation of sub-Recent mafic weathering profiles and Tertiary basaltic laterite and bauxite profiles is plotted as shaded circles (see text for references). The chemical index of alteration (CIA) and the index of lateritisation (IOL) may be integrated into both the A–CN–K and SAF ternary plots, respectively, as shown. In the SAF plot, the kaolinitisation and lateritisation boundaries are calculated from the chemistry of BB1 (parent rock of the Bidar profile).

Figure 6: (a) Comparison of the $MIA_{(O)}$ and CIA weathering indices for the Chhindwara and Bidar profiles, as well as the data compilation from Figure 5. (b) Plot of Fe^{2+}/Fe^{3+} vs. CIA for the Chhindwara profile demonstrating the progressive conversion of Fe^{2+} to Fe^{3+} in the basalt with increasing weathering intensity.

Figure 7: Molar ternary plots in Al–Fe–Mg–Ca–Na–K (AFMCNK) space. See Table 3 for molar oxide conversions. The (a) A–CNK–FM and (b) A–CNKM–F (A–L–F) plots were proposed by Nesbitt and Young (1989) and Nesbitt and Wilson (1992), respectively, while the (c) AF–CNK–M plot (shaded) is proposed in the present study. These diagrams expose the contribution of the mafic and felsic mineral components to rock weathering. The integration of the new mafic index of alteration (MIA) into AFMCNK space is illustrated; the A–CNK–FM plot, most suitable for studying weathering in reducing environments, is integrated with the $MIA_{(R)}$, while the A–L–F and AF–CNK–M plots are integrated with the $MIA_{(O)}$ for studying oxidative weathering trends.

In addition to the Chhindwara and Bidar samples, the data compilation from Figure 5 is plotted as well.

Figure 8: Co-variation of the loss on ignition (wt. %) with the (a) chemical index of alteration and (b) index of lateritisation. The calculated kaolinitisation and lateritisation boundaries from Figure 5b are shown on the latter. Strong correlations of the weathering indices with the loss on ignition during incipient to intermediate weathering (Chhindwara weathering profile) confirm the transformation of relatively anhydrous pyroxene and plagioclase to hydrous phyllosilicates (i.e., smectites and kaolinite). Over the much longer time scales of advanced weathering, Si is lost as these phyllosilicates are progressively altered to sesquioxides of Al and Fe. This trend is defined by a decreasing loss on ignition as the index of lateritisation increases.

Figure 9: Stratigraphic variation of the weathering indices ($MIA_{(O)}$ and CIA) (a) and mass balance (τ mass transport function) profiles of the alkaline earth (b) and alkali elements (c) for the Chhindwara weathering profile. The depth of the modern soil surface and the two individual lava flows are indicated. Mass balance calculations use Nb as the immobile index element and sample ChQB12 (depth of 140 cm) for the parent rock. Values less than 0 indicate a mass loss relative to the parent rock (up to 100 % or -1) while values greater than 0 are mass gains. Note the extreme enrichment in the alkali elements at the top of the lower flow (darker shading).

Figure 10: $\tau_{Nb,j}$ values vs. the CIA for the alkaline earth elements (plus Na and Li). Note that values below 0 (dotted line) represent a mass loss up to -1 (100 % depletion). The $\tau_{Nb,j}$ value of most elements is anti-correlated with the CIA indicating that they are mobile during the incipient to intermediate stages of weathering.

Figure 11: Normalised REE plots for the (a) upper and (b) lower flow of the Chhindwara profile and (c) the Bidar laterite. Note the change in scale between the two profiles. In each of the REE plots, the samples are normalised to the least-weathered (parent rock) samples (Table 4). Fractionation of the lanthanides is evident in the changes in the slope and the abundance relative to 1 (parent rock) in the plots. Highlighted for emphasis are Ce and Eu.

Figure 12: Fractionation of Sm/Nd ratio as a function of the CIA during the incipient and intermediate stages of Deccan Traps basalt weathering.

Figure 13: The fractionation of Eu from the trivalent REE, expressed as the Eu/Eu* ratio, is anti-correlated with the (a) CIA and the (b) Rb/Sr ratio, indicating the loss of Eu is strongly linked to that of Sr, Ca, and Na (i.e. plagioclase dissolution) during basalt weathering. The Eu/Eu* ratio is calculated following normalisation to the parent rock values (ChQB12 for Chhindwara profile and BB1 for Bidar profile). A Eu/Eu* value of 1 (dashed line) represents no Eu anomaly between Sm and Gd relative to the parent rock. The alkali element enriched samples from the Chhindwara profile (very high Rb/Sr) and the Bidar samples are not shown on the Rb/Sr plot.

Figure 1

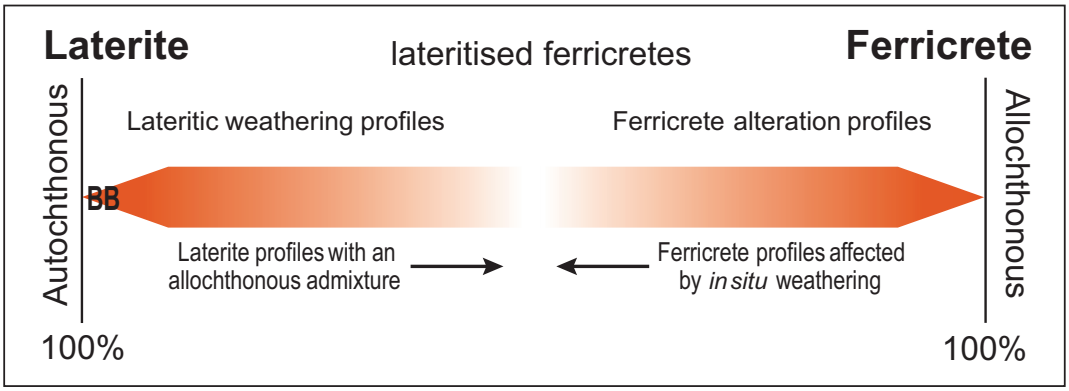
Laterite
lateritised ferricretes
Ferricrete
Autochthonous
Lateritic weathering profiles
Ferricrete alteration profiles
Allochthonous
BB
Laterite profiles with an allochthonous admixture
Ferricrete profiles affected by *in situ* weathering
100%
100%

Figure 2

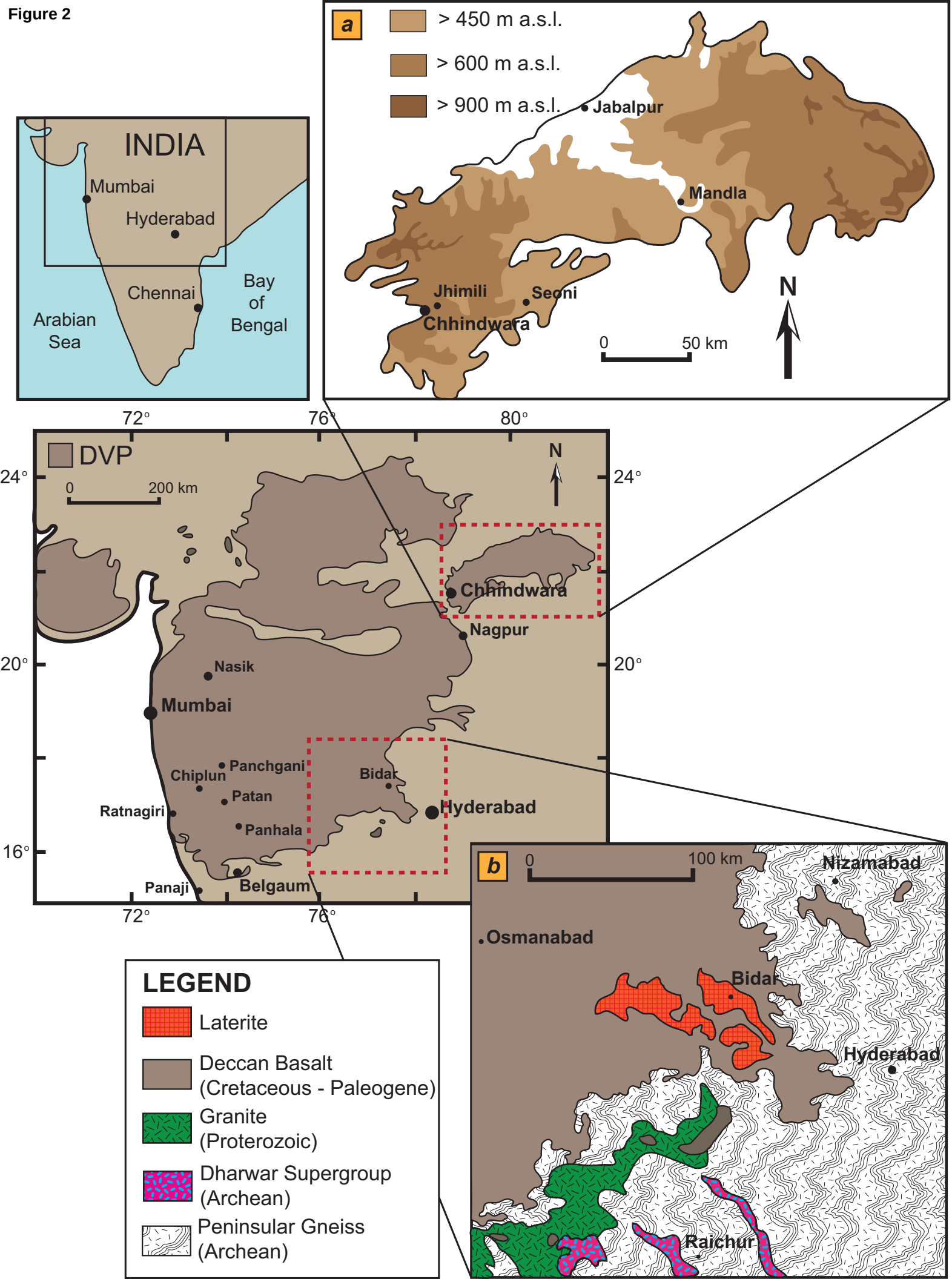
a
> 450 m a.s.l.
> 600 m a.s.l.
> 900 m a.s.l.
Jabalpur
Mandla
Jhimili
Seoni
Chhindwara
0
50 km
N
INDIA
Mumbai
Hyderabad
Chennai
Arabian Sea
Bay of Bengal
72°
76°
80°
24°
20°
16°
DVP
0
200 km
N
Chhindwara
Nagpur
Nasik
Mumbai
Panchgani
Chiplun
Patan
Ratnagiri
Panhala
Panaji
Belgaum
Bidar
Hyderabad
b
0
100 km
Nizamabad
Osmanabad
Bidar
Hyderabad
Raichur
LEGEND
Laterite
Deccan Basalt (Cretaceous - Paleogene)
Granite (Proterozoic)
Dharwar Supergroup (Archean)
Peninsular Gneiss (Archean)

Figure 3

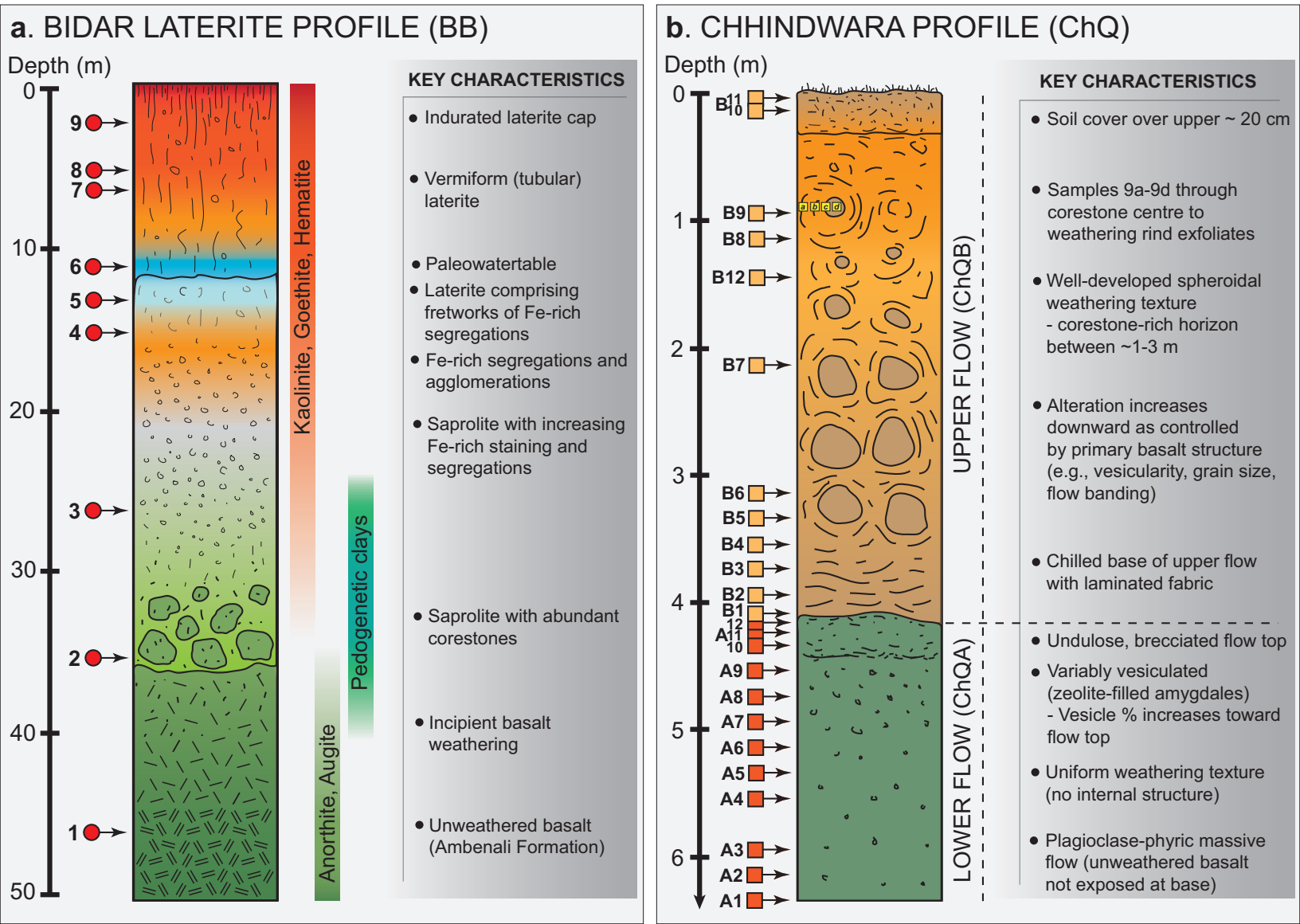
a. BIDAR LATERITE PROFILE (BB)
Depth (m)
0
10
20
30
40
50
9
8
7
6
5
4
3
2
1
Kaolinite, Goethite, Hematite
Pedogenetic clays
Anorthite, Augite
KEY CHARACTERISTICS
• Indurated laterite cap
• Vermiform (tubular) laterite
• Paleowatertable
• Laterite comprising fretworks of Fe-rich segregations
• Fe-rich segregations and agglomerations
• Saprolite with increasing Fe-rich staining and segregations
• Saprolite with abundant corestones
• Incipient basalt weathering
• Unweathered basalt (Ambenali Formation)
b. CHHINDWARA PROFILE (ChQ)
Depth (m)
0
1
2
3
4
5
6
B11
B10
B9
B8
B12
B7
B6
B5
B4
B3
B2
B1
A12
A11
A10
A9
A8
A7
A6
A5
A4
A3
A2
A1
UPPER FLOW (ChQB)
LOWER FLOW (ChQA)
KEY CHARACTERISTICS
• Soil cover over upper ~ 20 cm
• Samples 9a-9d through corestone centre to weathering rind exfoliates
• Well-developed spheroidal weathering texture
- corestone-rich horizon between ~1-3 m
• Alteration increases downward as controlled by primary basalt structure (e.g., vesicularity, grain size, flow banding)
• Chilled base of upper flow with laminated fabric
• Undulose, brecciated flow top
• Variably vesiculated (zeolite-filled amygdales)
- Vesicle % increases toward flow top
• Uniform weathering texture (no internal structure)
• Plagioclase-phyric massive flow (unweathered basalt not exposed at base)

Figure 4

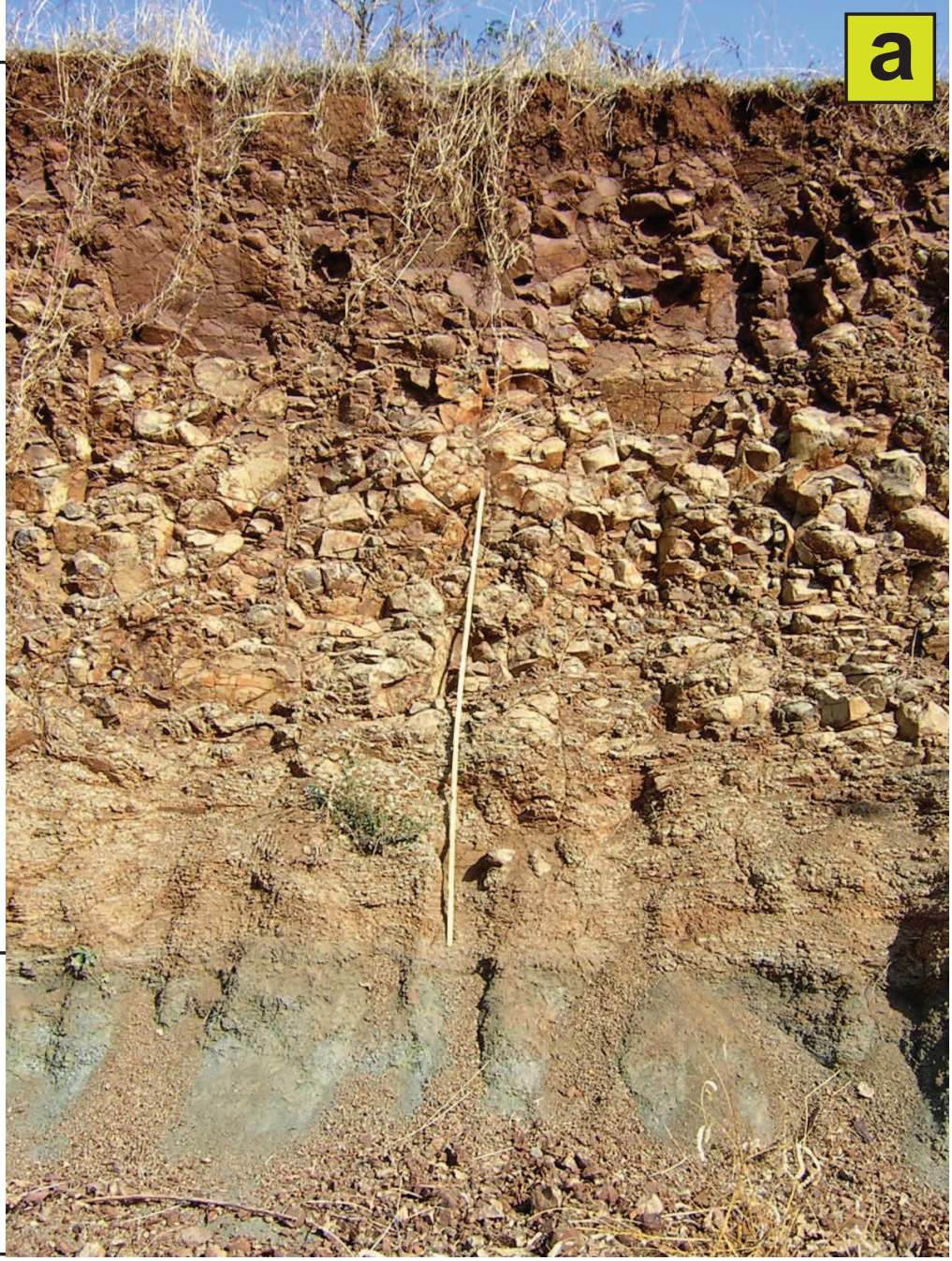

Figure 5

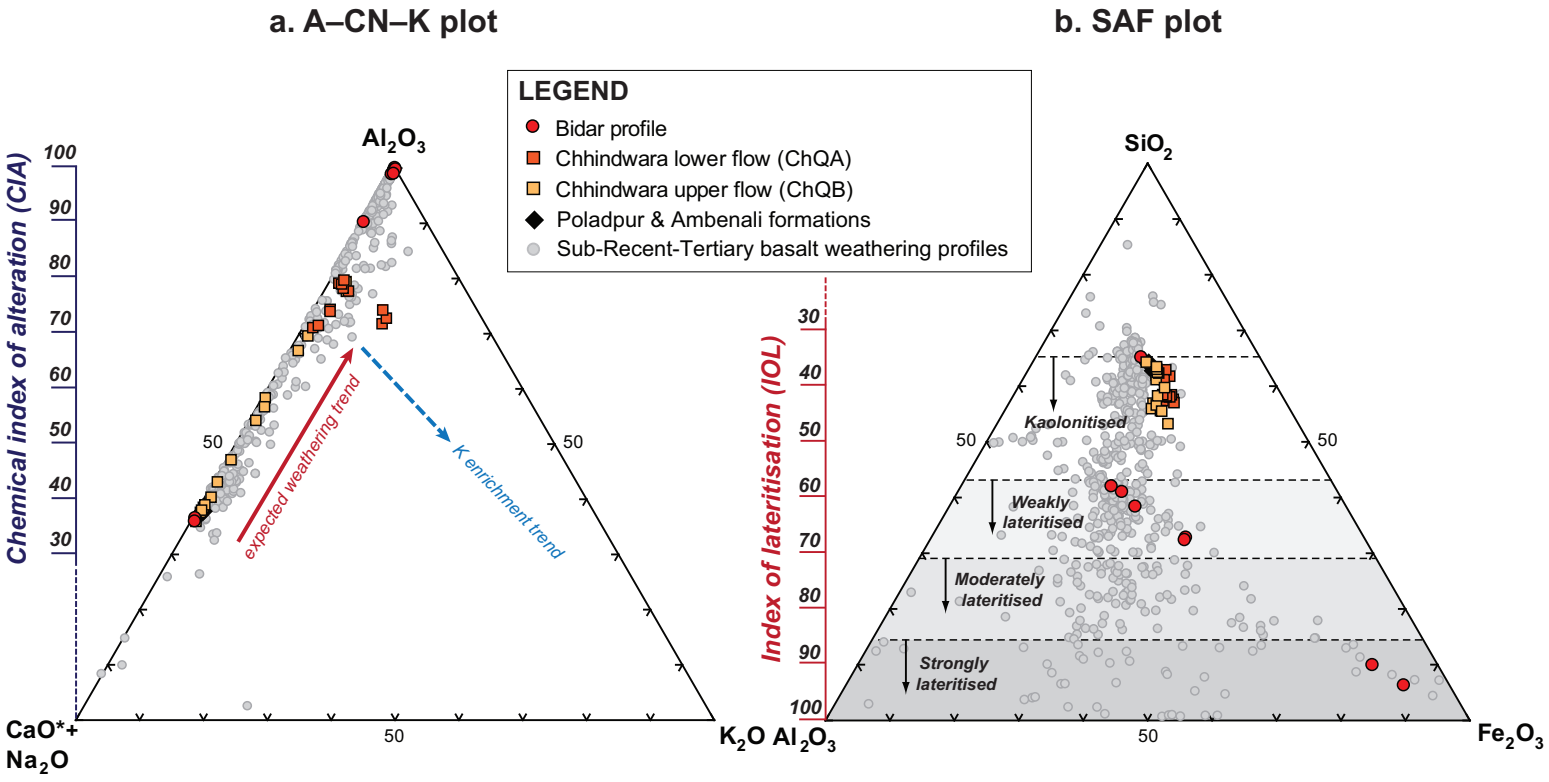
a. A–CN–K plot
b. SAF plot
LEGEND
Bidar profile
Chhindwara lower flow (ChQA)
Chhindwara upper flow (ChQB)
Poladpur & Ambenali formations
Sub-Recent-Tertiary basalt weathering profiles
Al2O3
CaO*+ Na2O
K2O Al2O3
Chemical index of alteration (CIA)
expected weathering trend
K enrichment trend
SiO2
Fe2O3
Index of lateritisation (IOL)
Kaolonitised
Weakly lateritised
Moderately lateritised
Strongly lateritised

Figure 6

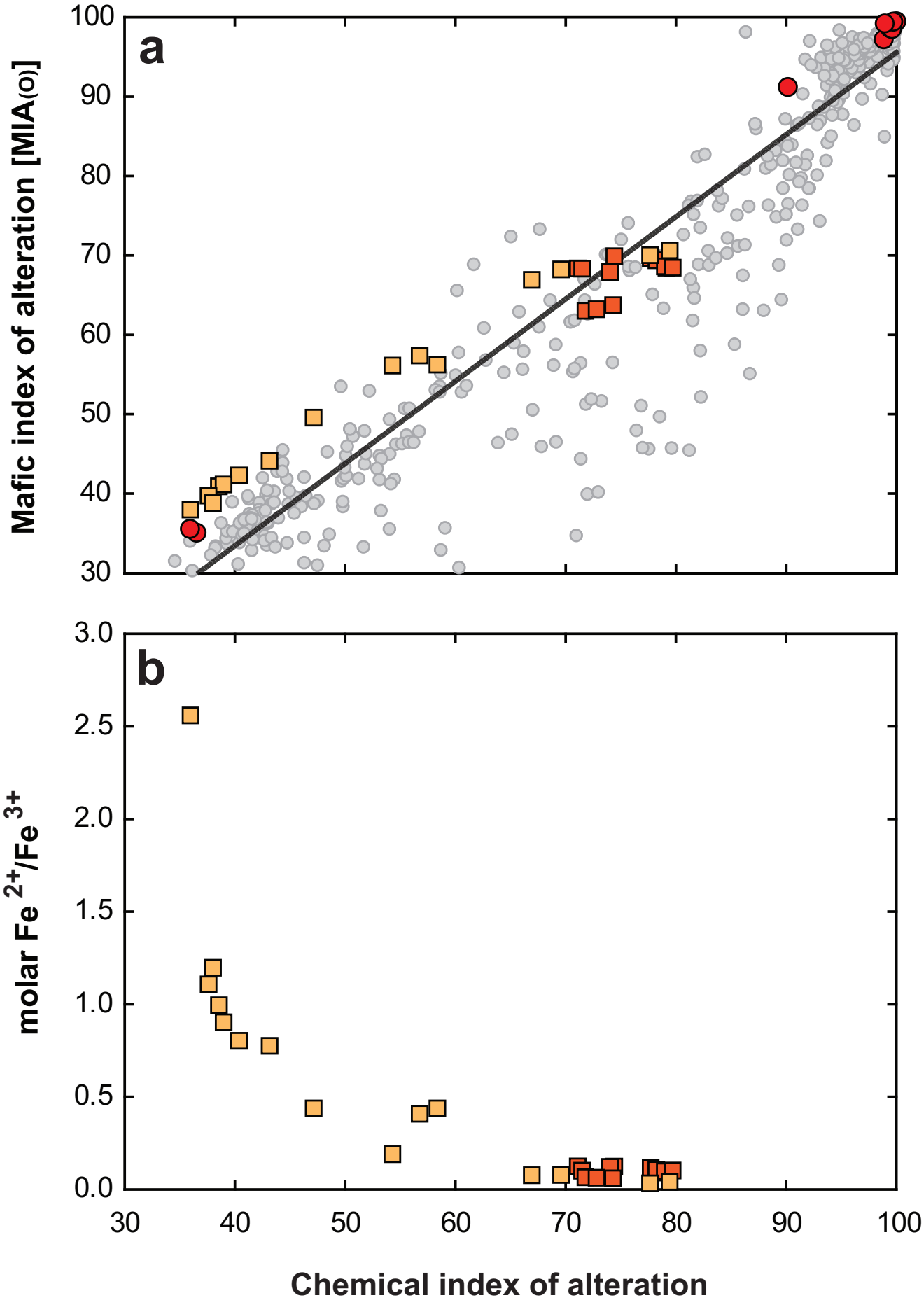
a
b
Mafic index of alteration [MIA(O)]
molar Fe2+/Fe3+
Chemical index of alteration
100
90
80
70
60
50
40
30
3.0
2.5
2.0
1.5
1.0
0.5
0.0
30
40
50
60
70
80
90
100

Figure 7

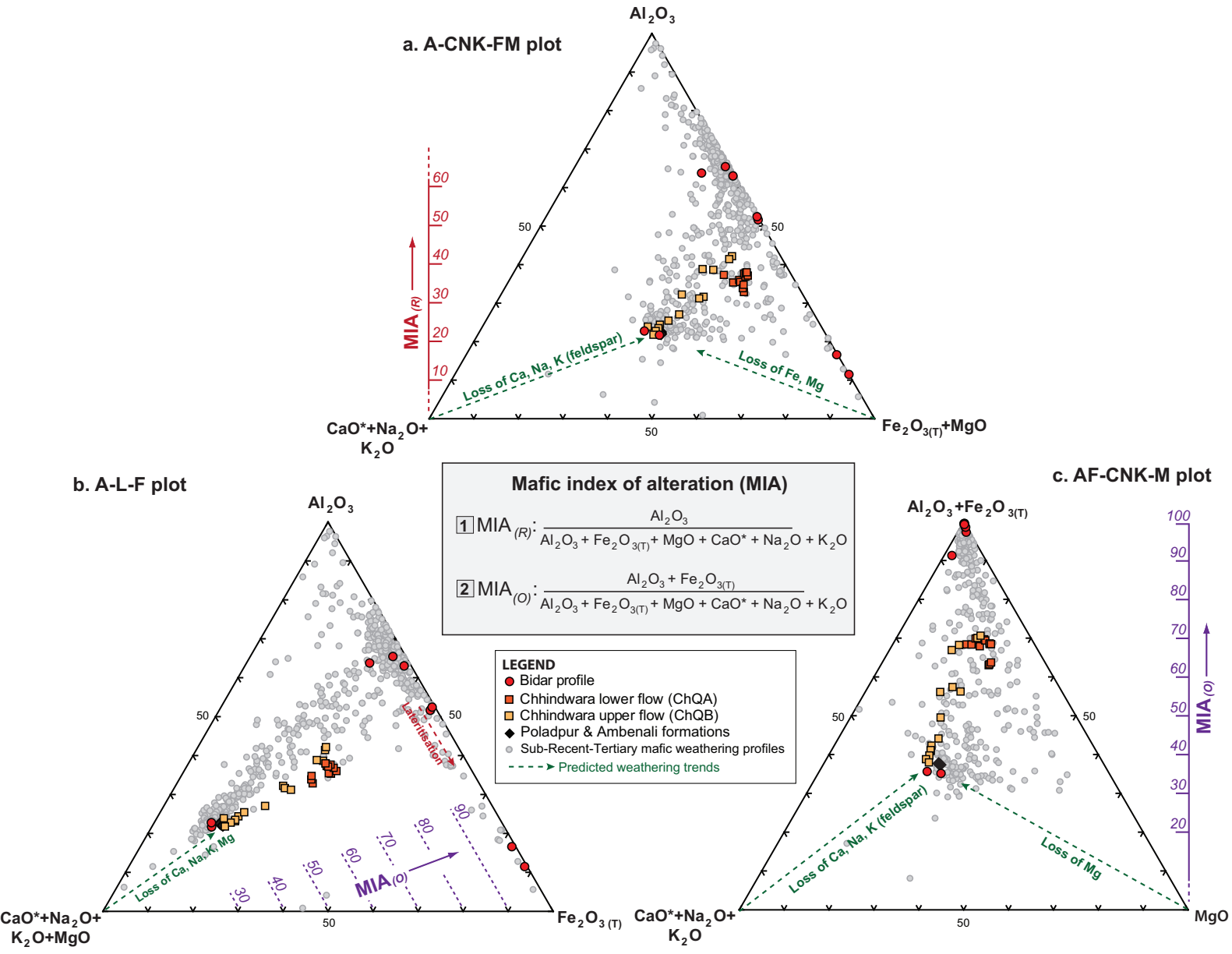
a. A-CNK-FM plot
Al_2O_3
$CaO^*+Na_2O+K_2O$
$Fe_2O_{3(T)}+MgO$
$MIA_{(R)}$
60
50
40
30
20
10
50
50
50
Loss of Ca, Na, K (feldspar)
Loss of Fe, Mg
b. A-L-F plot
Al_2O_3
$CaO^*+Na_2O+K_2O+MgO$
$Fe_2O_{3(T)}$
Laterisation
$MIA_{(O)}$
30
40
50
60
70
80
90
Loss of Ca, Na, K, Mg
c. AF-CNK-M plot
$Al_2O_3+Fe_2O_{3(T)}$
$CaO^*+Na_2O+K_2O$
MgO
$MIA_{(O)}$
100
90
80
70
60
50
40
30
20
Loss of Ca, Na, K (feldspar)
Loss of Mg
Mafic index of alteration (MIA)
1 $MIA_{(R)}: \frac{Al_2O_3}{Al_2O_3 + Fe_2O_{3(T)} + MgO + CaO^* + Na_2O + K_2O}$
2 $MIA_{(O)}: \frac{Al_2O_3 + Fe_2O_{3(T)}}{Al_2O_3 + Fe_2O_{3(T)} + MgO + CaO^* + Na_2O + K_2O}$
LEGEND
Bidar profile
Chhindwara lower flow (ChQA)
Chhindwara upper flow (ChQB)
Poladpur & Ambenali formations
Sub-Recent-Tertiary mafic weathering profiles
Predicted weathering trends

Figure 8

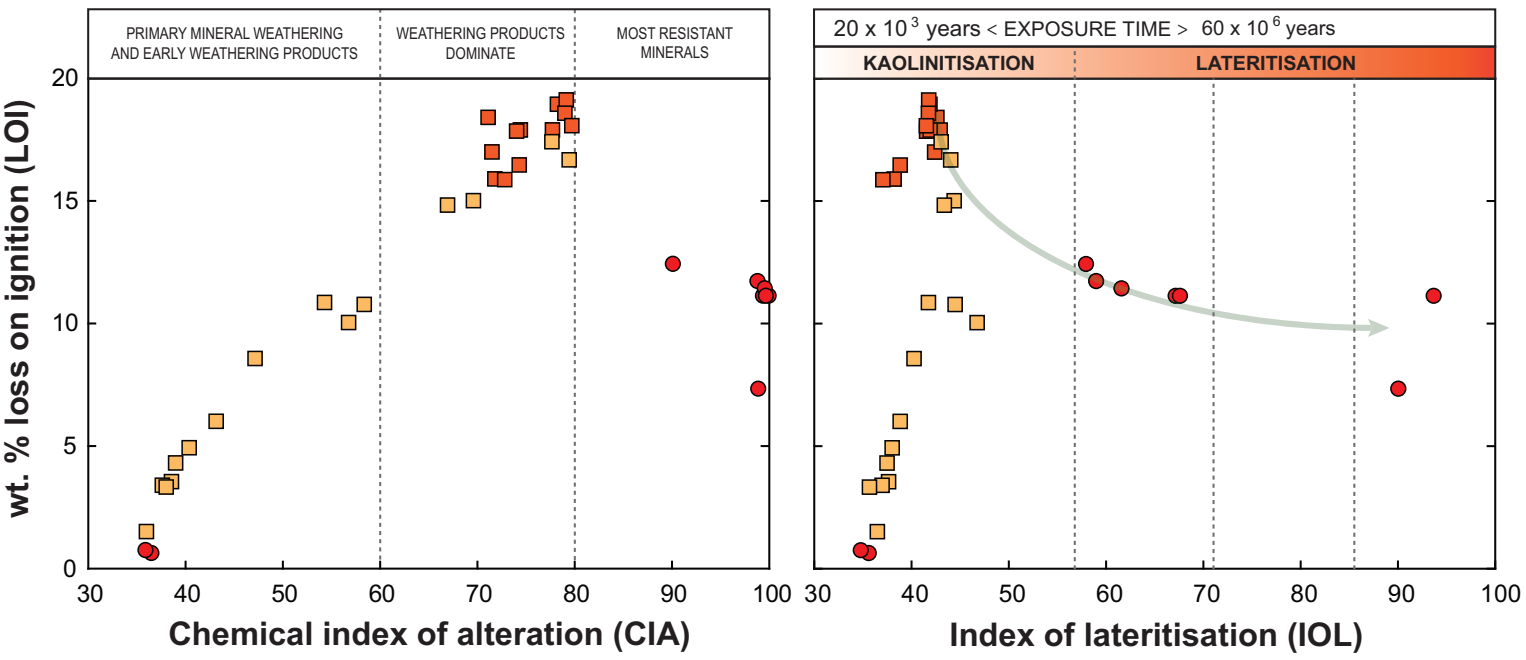
PRIMARY MINERAL WEATHERING AND EARLY WEATHERING PRODUCTS
WEATHERING PRODUCTS DOMINATE
MOST RESISTANT MINERALS
wt. % loss on ignition (LOI)
Chemical index of alteration (CIA)
20 x 10 3 years < EXPOSURE TIME > 60 x 10 6 years
KAOLINITISATION
LATERITISATION
Index of lateritisation (IOL)

Figure 9

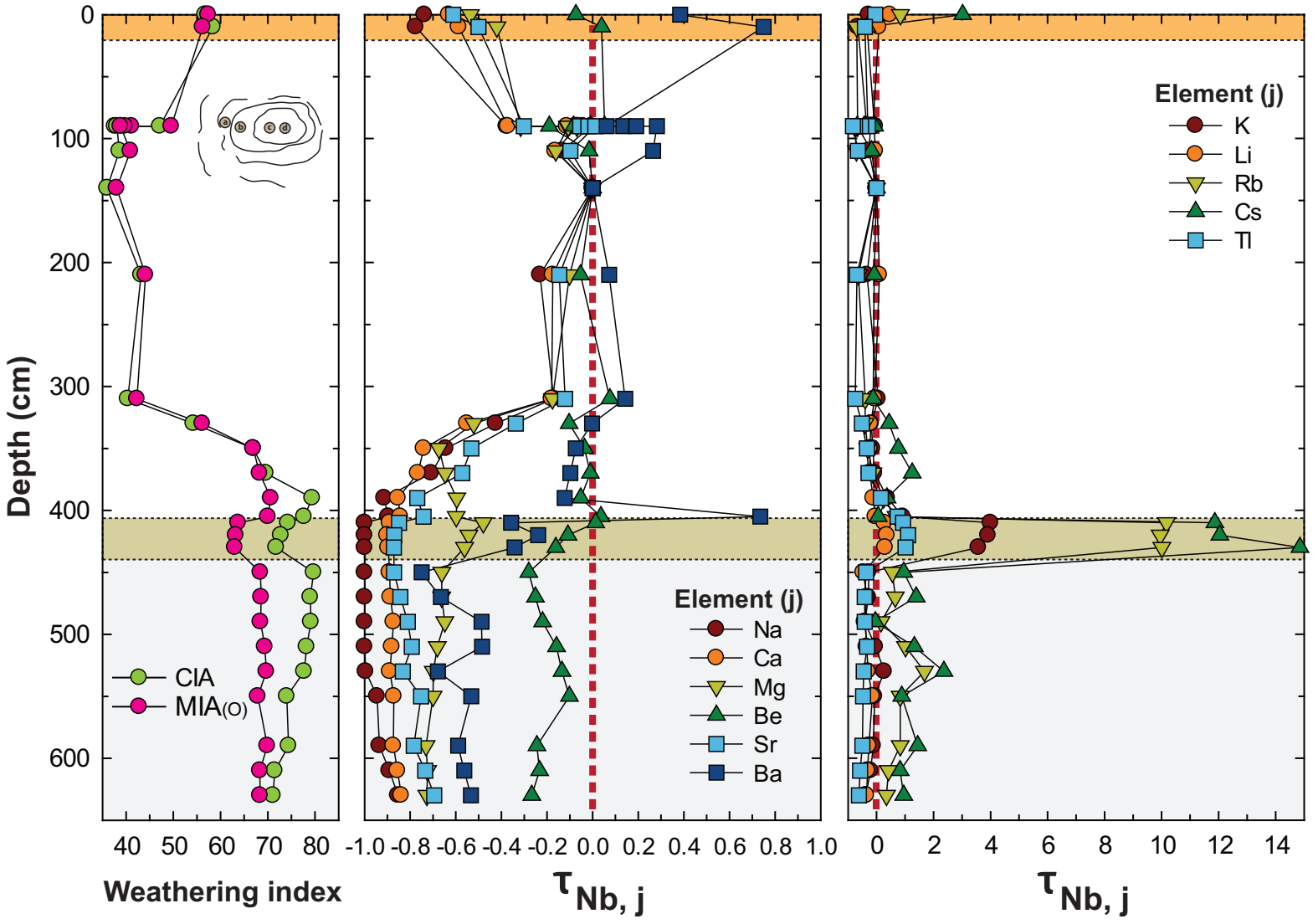
Depth (cm)
0
100
200
300
400
500
600
CIA
MIA(O)
40 50 60 70 80
Weathering index
Element (j)
Na
Ca
Mg
Be
Sr
Ba
-1.0 -0.8 -0.6 -0.4 -0.2 0.0 0.2 0.4 0.6 0.8 1.0
τNb, j
Element (j)
K
Li
Rb
Cs
Tl
0 2 4 6 8 10 12 14
τNb, j

Figure 10

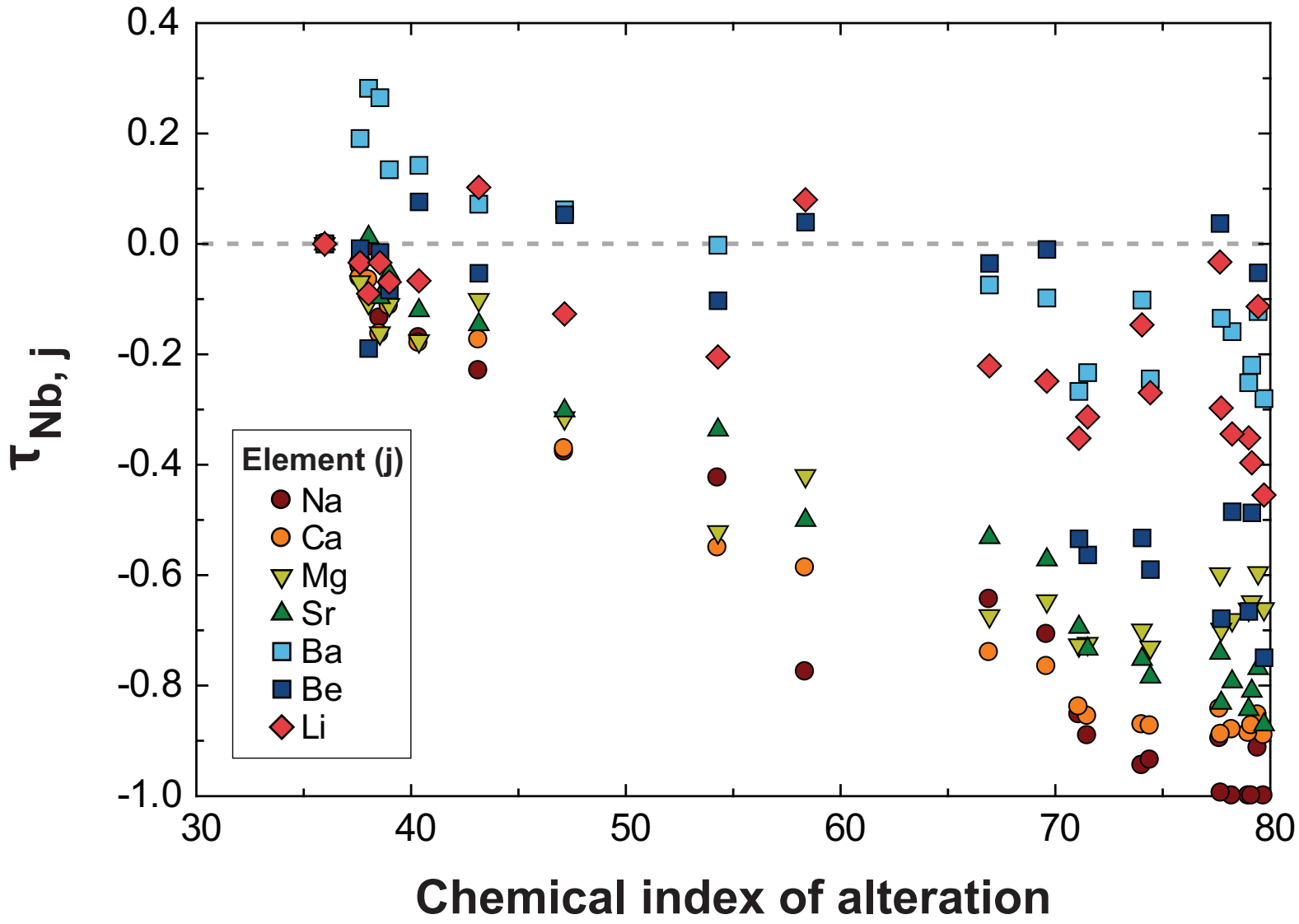
0.4
0.2
0.0
-0.2
-0.4
-0.6
-0.8
-1.0
30
40
50
60
70
80
τNb, j
Chemical index of alteration
Element (j)
Na
Ca
Mg
Sr
Ba
Be
Li

Figure 11

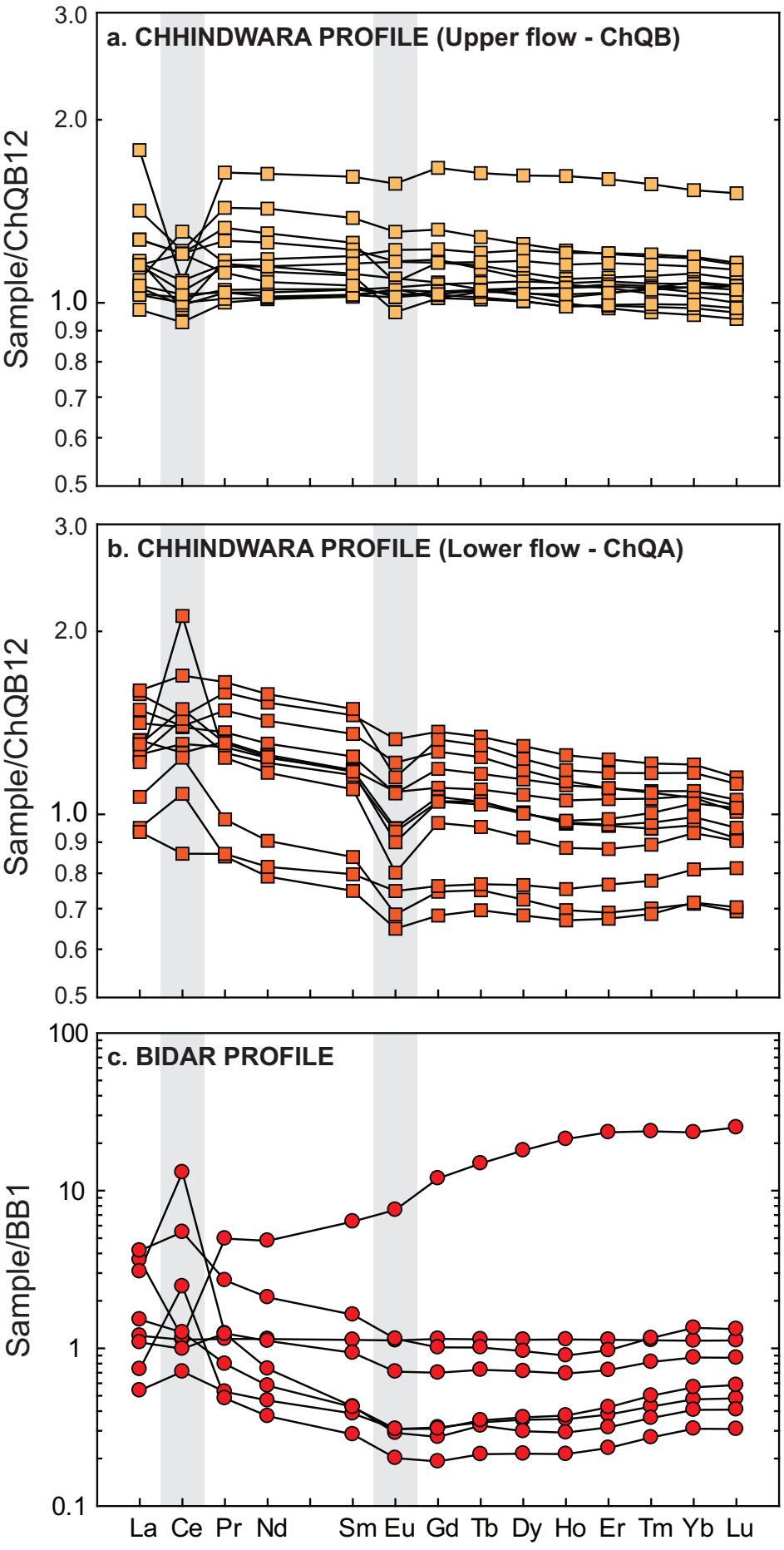
a. CHHINDWARA PROFILE (Upper flow - ChQB)
Sample/ChQB12
3.0
2.0
1.0
0.9
0.8
0.7
0.6
0.5
b. CHHINDWARA PROFILE (Lower flow - ChQA)
Sample/ChQB12
3.0
2.0
1.0
0.9
0.8
0.7
0.6
0.5
c. BIDAR PROFILE
Sample/BB1
100
10
1
0.1
La Ce Pr Nd Sm Eu Gd Tb Dy Ho Er Tm Yb Lu

Figure 12

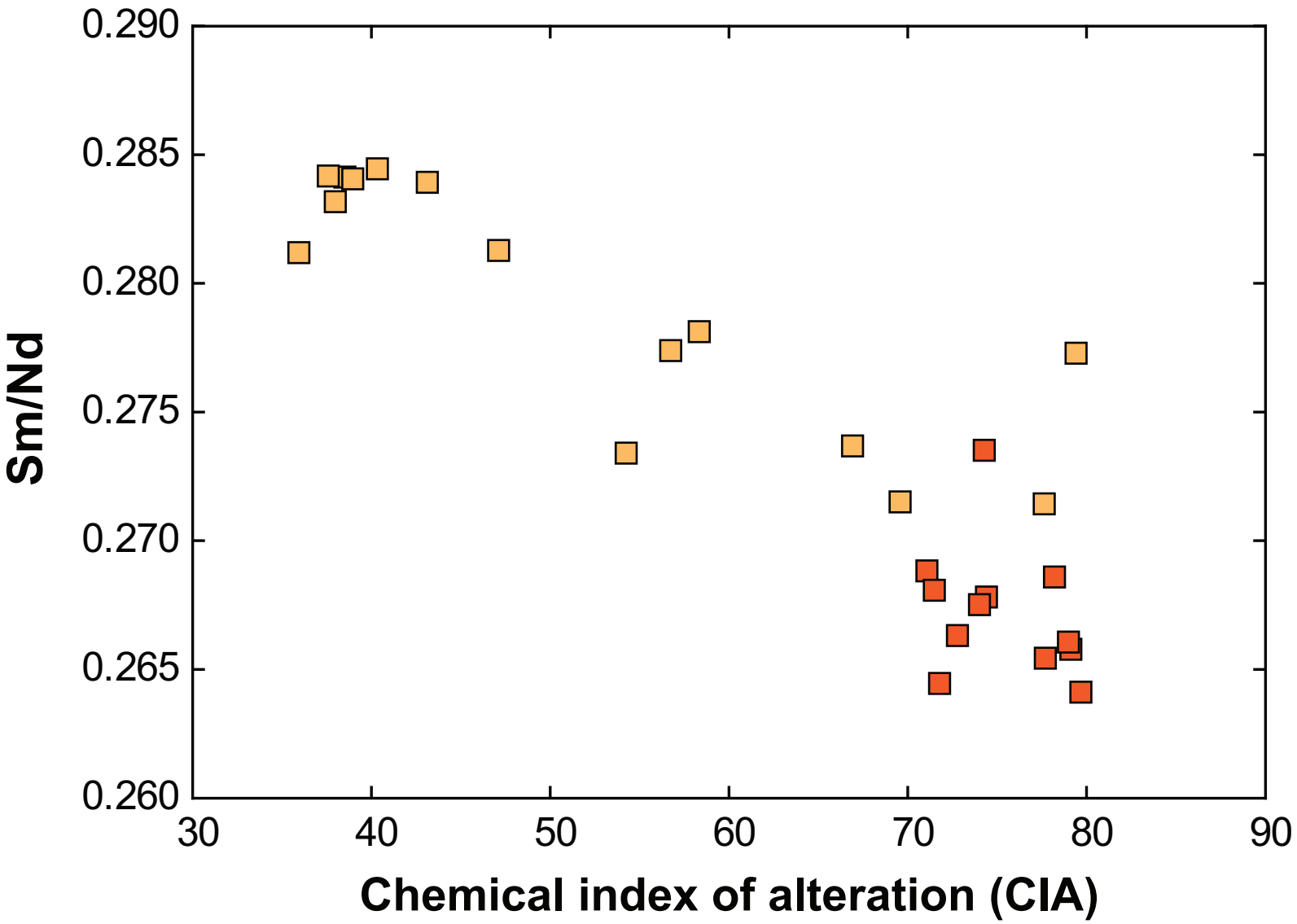
0.290
0.285
0.280
0.275
0.270
0.265
0.260
Sm/Nd
30
40
50
60
70
80
90
Chemical index of alteration (CIA)

Figure 13

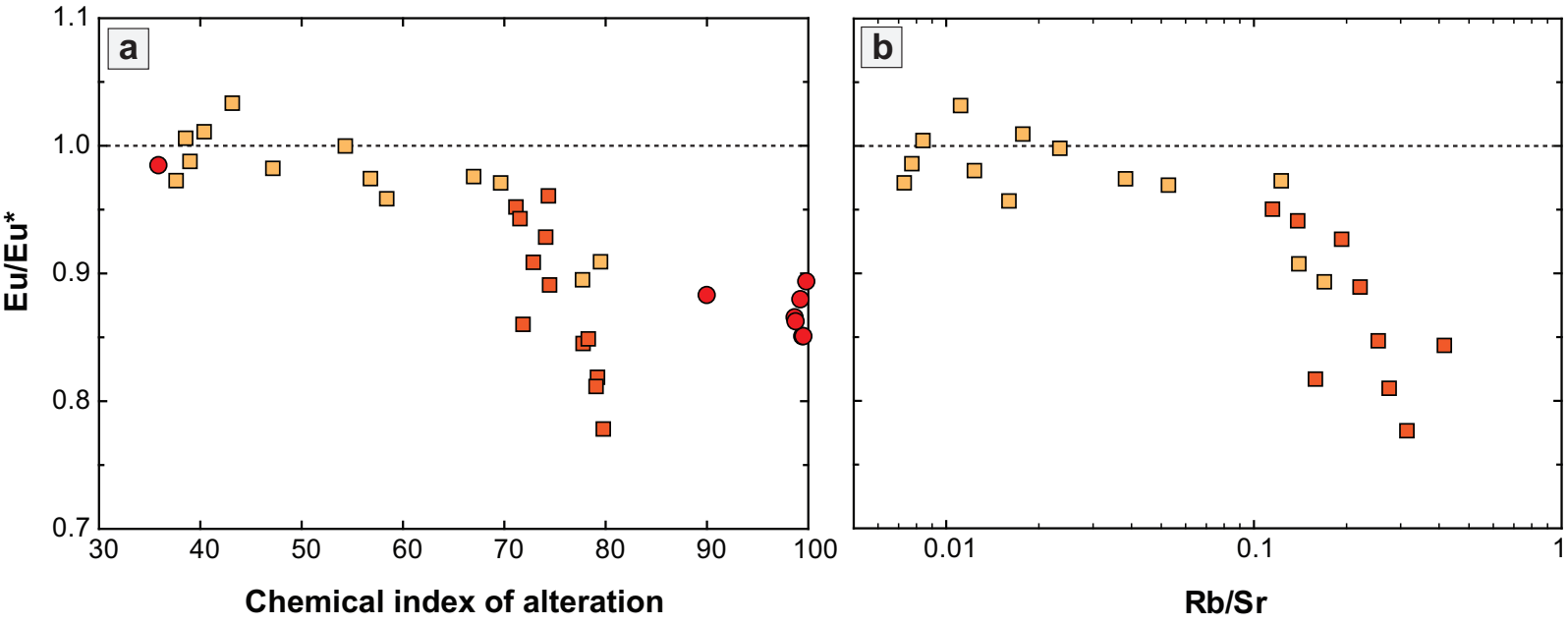
a
b
Eu/Eu*
1.1
1.0
0.9
0.8
0.7
30
40
50
60
70
80
90
100
Chemical index of alteration
0.01
0.1
1
Rb/Sr

Table 1

Click here to download Table: Table1_Bidardata.xlsx

Table 1: Major[a] (wt. %) and trace element (ppb) data for the Bidar (BB) laterite profile

	BB1	BB2	BB3	BB4	BB5	BB6	BB7
Depth (cm)	4700	3500	2600	1500	1300	1100	600
SiO_2	48.9	50.06	38.59	38.78	30.61	6.12	36.68
TiO_2	2.16	2.29	5.11	4.78	5.76	1.4	2.44
Al_2O_3	13.72	14.15	31.54	31.95	25.83	6.97	31.3
$Fe_2O_{3(T)}$	13.4	12.63	24.1	21.64	36.95	84.81	27.7
MgO	6.93	5.99	0.4	0.38	0.23	0.14	0.26
MnO	0.19	0.22	0.11	0.06	0.06	0.03	0.33
CaO	10.99	11.45	0.19	1.91	0.07	0	0.05
Na_2O	2.46	2.78	bdl	bdl	bdl	bdl	bdl
K_2O	0.16	0.25	0.02	0.01	0.02	0	0.03
P_2O_5	0.16	0.19	0.18	0.03	0.08	0.33	0.07
LOI	0.6	0.72	11.7	12.4	11.1	11.1	11.4
Total	99.07	100.01	100.24	99.54	99.61	99.8	98.86
CIA	37	36	99	90	99	100	100
$MIA_{(O)}$	35	36	97	91	99	99	98
IOL	36	35	59	58	67	94	62
Nb	9262	10202	18943	18600	23480	5646	14495
Li	4466	5159	7019	3736	4271	1202	13235
Rb	956	5678	1165	335	811	321	1524
Cs	8	221	114	68	102	37	142
Tl	3	24	8	16	29	7	272
Be	606	632	2435	1289	1319	3814	859
Sr	208492	227625	13746	23686	6022	46072	15494
Ba	50844	92866	59309	10603	16262	24813	398559
La	8587	10314	31316	4642	9357	35766	26386
Ce	21805	24700	25511	15509	21649	119190	285003
Pr	3250	3729	16136	1724	4044	8776	4007
Nd	15508	17765	74513	7240	17296	32632	11510
Sm	4448	5035	28324	1717	4166	7276	1901
Eu	1592	1786	12010	490	1134	1832	463
Gd	5264	6039	62888	1657	3688	5340	1444
Tb	850	968	12625	288	620	859	274
Dy	5083	5758	91424	1791	3642	4878	1516
Ho	1028	1170	21863	365	712	926	300
Er	2688	3047	63014	1022	1956	2614	848
Tm	379	425	9016	162	310	440	137
Yb	2290	2556	53585	1087	2003	3089	933
Lu	321	360	8079	155	280	425	131

[a] Major element data has been recalculated without the LOI as reported in Borger and Widdowson (200

Table 2

Click here to download Table: Table2_Chhindwaradata.xlsx

Table 2: Major (wt. %) and trace element (ppb) data for the Chhindwara (ChQ) weathering profile

	Lower flow (ChQA)												Upp						
	ChQA1	**ChQA2**	**ChQA3**	**ChQA4**	**ChQA5**	**ChQA6**	**ChQA7**	**ChQA8**	**ChQA9**	**ChQA10**	**ChQA11**	**ChQA12**	**ChQB1**	**ChQB2**	**ChQB3**	**ChQB4**	**ChQB5**	**ChQB6**	**ChQB7**
Depth (cm)	630	610	590	550	530	510	490	470	450	430	420	410	405	390	370	350	330	310	210
SiO_2	40.91	41.7	41.02	42	41.99	41.38	41.23	41.72	41.98	45.44	46.92	45.14	41.76	41.43	41.29	42.14	43.69	46.95	46.35
TiO_2	2.97	3.03	3.1	3.03	3.1	2.92	2.91	2.91	3.04	2.52	2.43	2.27	2.58	2.72	2.59	2.67	2.55	2.32	2.23
Al_2O_3	13.19	12.46	12.5	12.28	12.66	12.87	13.08	12.86	13.23	11.53	11.72	12.44	15.16	15.85	14.99	15.14	14.48	13.39	13.7
$Fe_2O_{3(T)}$	17.18	18.21	18.39	17.59	17.65	16.97	16.5	17.04	16.59	16.57	15.91	16.23	16.4	16.74	17.97	17.14	16.82	15.4	15.73
MgO	2.3	2.45	2.43	2.69	2.68	2.72	2.94	2.94	3.01	3.34	3.3	3.43	2.61	2.74	2.28	2.14	2.97	4.71	4.75
MnO	0.21	0.25	0.26	0.21	0.15	0.22	0.27	0.22	0.25	0.18	0.22	0.2	0.39	0.38	0.31	0.31	0.26	0.21	0.22
CaO	2.62	2.47	2.2	2.23	1.91	1.97	2.05	1.9	1.88	1.53	1.39	1.4	1.97	1.92	2.92	3.29	5.39	9.06	8.43
Na_2O	0.55	0.43	0.26	0.22	0.02	bdl	bdl	bdl	bdl	bdl	bdl	bdl	0.3	0.26	0.84	1.04	1.59	2.11	1.81
K_2O	0.27	0.36	0.41	0.43	0.58	0.42	0.25	0.32	0.33	1.79	1.82	1.69	0.64	0.48	0.31	0.29	0.26	0.31	0.18
P_2O_5	0.25	0.26	0.24	0.24	0.21	0.19	0.23	0.16	0.17	0.08	0.05	0.03	0.17	0.14	0.2	0.22	0.21	0.21	0.19
LOI	18.41	17	17.9	17.85	17.9	18.95	19.12	18.58	18.07	15.9	15.87	16.47	17.42	16.68	15.01	14.83	10.86	4.93	6.01
Total	98.86	98.61	98.71	98.78	98.86	98.59	98.57	98.58	98.56	98.8	99.55	99.24	99.4	99.33	98.69	99.2	99.1	99.59	99.59
CIA	71.1	71.5	74.4	74.0	77.7	78.2	79.1	79.0	79.7	71.8	72.8	74.3	77.7	79.4	69.6	66.9	54.3	40.4	43.2
$MIA_{(O)}$	68.4	68.3	69.9	67.9	69.7	69.4	68.5	68.6	68.4	63.0	63.2	63.7	70.0	70.6	68.2	66.9	56.1	42.3	44.1
IOL	42.6	42.4	43.0	41.6	41.9	41.9	41.8	41.7	41.5	38.2	37.1	38.8	43.0	44.0	44.4	43.4	41.7	38.0	38.8
Nb	13180	13899	14128	14051	13917	13349	13098	13618	13913	11945	11309	10323	10170	10624	10117	10283	9728	8956	8279
Li	5704	6372	6893	8006	6533	5848	5279	5899	5066	10434	10340	8789	6570	6290	5076	5351	5167	5583	6094
Rb	10864	12050	15799	15731	22796	16426	9251	13773	13240	80357	75652	70446	10458	8058	5368	4333	3551	3287	1853
Cs	267	263	357	274	485	321	130	337	281	1963	1528	1377	111	150	236	188	145	82	79
Tl	27	32	38	40	41	48	41	43	47	130	128	107	95	66	39	37	25	12	14
Be	775	855	856	1013	966	901	820	818	803	803	809	839	846	807	803	795	700	773	629
Sr	94861	87125	71695	81898	55065	65039	58589	50272	42335	36116	34676	36638	61940	57762	101971	113398	151897	185479	166489
Ba	59973	59279	56571	64124	43629	67110	65604	44466	34010	76707	84039	64761	172384	91068	89129	93009	94793	99949	86700
La	13548	17025	15254	16040	14299	13477	17268	14072	13164	11535	10258	10102	13727	11770	15305	13708	12561	12656	10515
Ce	34976	38794	37273	37426	33825	38470	45309	39896	56787	33206	28956	23082	32294	35068	32617	32288	29134	26217	24891
Pr	4998	6149	5290	5747	5107	4893	6398	5074	4803	3803	3305	3338	5150	4507	5556	4901	4488	4549	3880
Nd	22625	27902	23884	26045	22892	22198	28810	22702	21390	16530	14438	14972	23765	20549	26090	22962	20970	21562	18519
Sm	6081	7479	6395	6966	6075	5961	7656	6039	5648	4371	3844	4095	6450	5697	7083	6283	5732	6133	5258
Eu	1969	2404	1958	2200	1717	1694	2082	1628	1451	1238	1173	1353	1956	1745	2367	2116	1984	2209	1906
Gd	6750	8345	7248	7737	6520	6412	8106	6401	5907	4553	4161	4652	7109	6210	8054	7185	6593	7475	6212
Tb	1092	1333	1158	1234	1043	1043	1290	1031	947	745	691	763	1144	1036	1274	1130	1046	1201	1006
Dy	6525	7847	6916	7167	6100	6083	7476	6074	5550	4387	4133	4635	6789	6297	7569	6657	6226	7396	6090
Ho	1313	1559	1391	1413	1204	1208	1473	1216	1097	867	834	939	1364	1272	1518	1334	1243	1505	1229
Er	3516	4085	3666	3666	3180	3193	3884	3260	2911	2287	2236	2543	3652	3441	3992	3510	3250	4005	3283
Tm	502	574	516	513	448	459	553	476	422	331	324	368	524	500	564	489	456	568	466
Yb	3112	3503	3168	3088	2783	2870	3395	3024	2702	2068	2078	2356	3241	3138	3433	2970	2769	3453	2842
Lu	427	476	437	417	378	393	464	424	374	286	291	337	453	441	477	413	389	481	398

Table 3
Click here to download Table: Table3_MoleConversions.xlsx

Table 3: Mole conversions for weathering index calculations

moles Al_2O_3 = wt % Al_2O_3 ÷ 101.96
moles Fe_2O_3 = wt % *Fe_2O_3 ÷ 159.69
moles FeO = wt % FeO ÷ 71.84
moles MgO = wt % MgO ÷ 40.30
moles CaO = wt % CaO ÷ 56.08
moles Na_2O = wt % Na_2O ÷ 61.98
moles K_2O = wt % K_2O ÷ 94.20
moles P_2O_5 = wt % P_2O_5 ÷ 141.94
moles CO_2 = wt % CO_2 ÷ 44.01

$$CaO^* = \text{moles CaO} - \text{moles } CO_{2\ (\text{calcite})} - (0.5 \times \text{moles } CO_2)_{\ (\text{dolomite})} - [(10/3) \times \text{moles } P_2O_5]_{\ (\text{apatite})}$$

---

*wt % Fe_2O_3 = wt % FeO wt ÷ 0.8998

Table 4
Click here to download Table: Table4_weatheringindexvaluesforfreshrocks.xlsx

Table 4: Weathering index values for mafic standards and parent rock samples

Sample			
USGS[a]	**CIA**	**$MIA_{(O)}$**	**IOL**
BIR-1	36.3	30.5	35.8
BHVO-2	35.7	33.4	34.1
BCR-2	41.2	44.1	33.5
W-2	39.5	36.0	33.3
DNC-1	43.2	33.2	37.5
Parent rocks			
BB-1	36.5	35.0	35.7
ChQB12	36.0	38.0	36.5
ChQB9d (corestone centre)	38.0	38.8	35.7
Deccan Traps (Widdowson et al., 2000)			
average Poladpur formation	37.8	37.1	35.9
average Ambenali formation	37.2	37.4	37.2

[a]weathering index values were calculated using the accepted values for the USGS standards

Background dataset for online publication only

Click here to download Background dataset for online publication only: Babechuketal_SupplementaryInformation.pdf

Background dataset for online publication only

Click here to download Background dataset for online publication only: SupplementaryTable1.xlsx

Background dataset for online publication only

Click here to download Background dataset for online publication only: SupplementaryTable2_Limit of kaolinitisation.xlsx